MONTANUNIVERSITÄT LEOBEN

Development of hard coatings for press hardening processes

Diploma Thesis

Christian Maringer
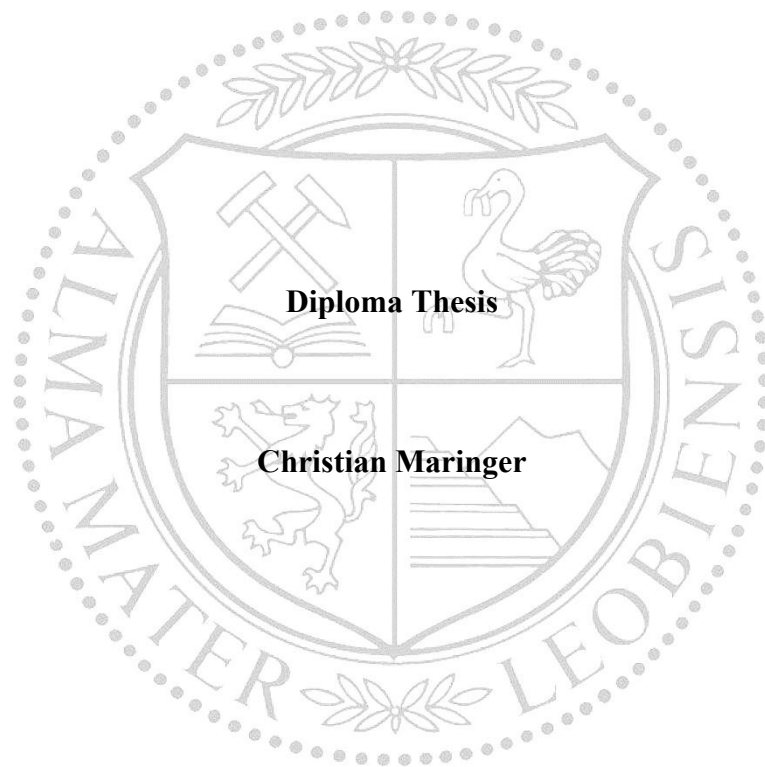
This thesis has been prepared at the Department of Physical Metallurgy and Materials Testing in cooperation with OC Oerlikon Balzers AG, Liechtenstein.

Leoben, 21.06.2011

Affidavit

I declare in lieu of oath that I did the diploma thesis by myself using only the literature cited in this volume.

Leoben, 21.06.2011   (Christian Maringer)

Acknowledgements

This diploma thesis would not have been possible without the support of many people. At this point I want to use the opportunity to express my gratitude to them.

First, I want to thank OC Oerlikon Balzers AG and their decision makers for the opportunity to write my diploma thesis there. Especially I want to thank my advisor Dr. Arnd Müller and my college Dr. Matthias Sobiech. The generous clearance during my diploma thesis facilitated my personal development and prepared me for further challenges.

A person I really owe gratitude is Assoz.-Prof. DI Dr. Paul Mayrhofer, who supported me since the physical metallurgy courses. Everything started with my position as student assistant, whereby he inspired my interests in thin film technology. Furthermore, Paul gave me the opportunity for a sojourn in the United States, where I learned a lot. During these years he impressed me by his natural manner on the one side and the competence in research on the other side. It was a pleasure to work for and with him.

Furthermore, my thank goes to my colleges at Balzers, especially DI Markus Lechthaler, who became a good friend during the 7 months I spent there. He was a source of inspiration, in work related topics as well as free time. Next to Markus my thanks go to Dr. Mirjam Arndt, Klaus Albrecht, and my unknown twin Dr. Denis Kurapov. All of you were on hand with help and advice for me and gave me a great time in Liechtenstein.

I am particularly obliged to my friends, first and foremost to DI Stefan Vollgger, Ernst Plesiutschnig and DI Patrick Christian Bürßner. During the years at University they have been my studying colleges, expedition members, espresso partners, ancillary workers or just my best friends.

Ganz besonders möchte ich an dieser Stelle auch meiner Familie danken. Durch deren Unterstützung war es mir erst möglich meine Studienzeit so zu gestalten, wie ich es richtig erachtet habe, sei es nun in Studienbelangen oder auch in außeruniversitären Tätigkeiten.

Table of contents

Table of figures

List of tables

List of abbreviations

CVD	chemical vapour deposition
PACVD	plasma assisted chemical vapour deposition
PVD	physical vapour deposition
DC	direct current
SZM	structure zone model
SRV	oscillation-friction-wear
XRD	x-ray diffraction
SEM	scanning electron microscope
EDX	energy dispersive x-ray spectroscopy
BSE	back scattered electron investigation
et al.	et alii means and others

1 Introduction

The last decade in automotive industry has been strongly influenced by two topics: First were the fast economic developments with increasing energy prices, and second, the discussion about the climate change. Influenced by these developments and new regulations for the future, the automotive manufactures have been forced to design new cars with less fuel consumption.

One efficient way to reach this goal is to reduce the cars weight. This can be done via the utilization of light metals e.g. aluminium or magnesium alloys. However, these metals have very energy intense production processes, compared to steel. Another solution is the utilization of high strength steels e.g. USIBOR® 1500 [1]. These steels, as many others too, exhibit the highest strength with a fully martensitic microstructure. In conventional processing a heat treatment is necessary after forming. Nevertheless, it is more economical to form these steels at high temperature. For protection of scaling and lubrication during forming, the steel sheets are covered by a protective layer. According to Oerlikon Balzers, the press hardening dies are sheltered with hard coatings e.g. ALCRONA (Al-Cr-N) or LUMENA (Ti-Al-N) for wear reduction.

These coating systems are characterized by their high hardness and wear resistance. However, they also show some disadvantages in this complex application. One of these observed issues is the deposition of a smeared metal layer from the coated steel sheets on the coatings surface. These deposits enlarge the required forming force, reduce the surface quality of the formed steel sheet and lead to adhesive wear at the coated forming tools in press hardening processes.

During the press hardening process a steel sheet is formed and heat treated in one step, see Figure 1.1. Therefore, the cut steel sheet, also called board, becomes heated up in an oven up to a temperature T ≈ 950 °C. At this temperature the microstructure has changed into austenite. The austenitic board is moved into the moulding die, where it becomes formed. For generation of a martensitic microstructure after forming, the moulding die is cooled. Thus, the steel sheets become quenched during forming, the change in microstructure takes place and components with highest strength are produced. In modern cars these components are in use for side impact bars, B-pillars and more security relevant components [2].
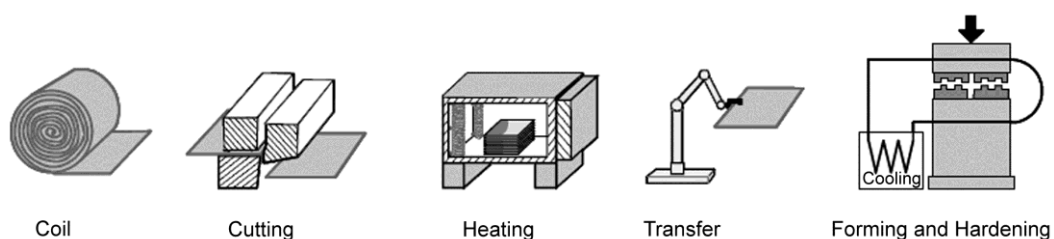
Figure 1.1: Process chain of press hardening for forming of hardenable high-strength steels [2].

In this thesis new coating systems have been prepared, investigated and compared with the already known systems. Basically, the new systems should improve the smeared metal effect during press hardening. Other properties in focus are hardness, thermal stability and oxidation resistance, wear resistance, friction behaviour and the adhesion to the substrate.

For characterization of the smeared metal effect, different measurements and characterization methods have been used. Already realised investigations have shown an influence of the surface energy on the adhesion behaviour of the coating. Hence, contact angle measurements were used to define the surface energy. Other investigation methods were high temperature oscillation-friction-wear tester (SRV tester) and hardware tests. Detailed descriptions to these specific methods can be found in chapter 3.

2 Deposition of coatings

Isaac Newton: "What we know is a drop, what we don't know is an ocean" [3].

2.1 General

The lifetime and the properties of components are significantly influenced by their surface. Due to the circumstance, the components surface interacts with other surfaces or the environment. Consequently, by surface modification, properties can be improved with respect to friction, wear, corrosion, appearance etc. This connection leaded, among other things, to the development of several different coating processes during the last few decades. Hence, many processes exist today [4]. The following figure gives an overview of some different coating technologies.

Table 1: Overview of different coating processes [4].

coating principle	adhesion generated by	coating processes
mechanical	high pressure	- roll gladding - explosion gladding, etc.
thermo-mechanical	Remelting of surface and application of force	- flame spraying - plasma spraying, etc.
thermal	Melting of surface	- deposition welding - hot dipping - deposition sintering, etc.
chemical	Modification of chemical composition on the surface	- phosphating - sol-gel deposition, etc.
electro-chemical	Bonding on atomic scale	- coating of Copper, Chrome, Zinc, Nickel, etc.
vapour deposition	Bonding on atomic scale	- physical vapour deposition - chemical vapour deposition - plasma assisted CVD

The major vapour coating processes for industrial hard coatings are the physical vapour deposition (PVD) and the chemical vapour deposition (CVD). In CVD processes gaseous chemical reactants are passed into the reaction chamber, where they become activated thermally (conventional CVD) or by other possibilities like plasma (plasma assisted CVD) or by laser beam (laser induced CVD). Chemical reactions of the activated reactants build up the coating on the substrates surface. The properties of the coating are strongly influenced by the process parameters. An issue of CVD processes is the low range of variation of the process parameters compared to PVD processes. Nevertheless, CVD coatings are signalized by their uniform thickness, even on complex geometries, a low porosity and a high purity. Therefore CVD coatings are often used in semiconductor industries.

The basic PVD processes can be divided by the method to transfer the target material into the gaseous state. Two basic PVD processes can be identified: first sputtering and second evaporation. In both processes a plasma is generated, which is of major importance for the properties of the deposited coating [5]. An exceptional position has the electron beam evaporated PVD, whereby no plasma is generated [6].

2.2 Plasma

2.2.1 Definition, properties and characteristic values of plasma

Generally, a plasma is defined as a quasineutral gas, which consists of electrons, ions and neutrals and exhibits a collective behaviour in an electromagnetic field. As a result of its behaviour and distinction from the other three states of matter, solid, liquid and non-ionized gas, plasma is also called the fourth state of matter. As with the other three states of matter, the density is one characterization parameter often in use. The plasma density n is defined as the number of charged species in a volume (usually cm^3). For equilibrium state the densities of electrons (n_e) and ions (n_i) are assumed to be equal. Furthermore the fraction of ionization can be defined as $f_i = n_e/(n_e+n_0)$, with n_0 as density of neutral species [7].

The energies of plasma particles (E) are simply linked with the effective temperature (T) by $T = E/k_B$. However, the temperatures of electrons (T_e), ions (T_i) and non-charged particles (T_n) can differ drastically from the plasma temperature (T_p). These differences are reasonable due to different mass and modes of motion. In thermodynamic equilibrium the temperatures of different species are about the same, $T_e = T_i = T_p$ [6]. Technical plasmas are not in thermodynamic equilibrium, which is desired.

Debye length (λ_D)

The Debye length describes the shielding of Coulomb potentials of charged particles. Inside λ_D, the potential of ion decrements to 1/e from the original potential and is defined as [8]:

$$\lambda_D = \sqrt{\frac{\varepsilon_0 \cdot k_B \cdot T_e}{n_e \cdot e^2}},$$ (2.1)

where ε_0 is the vacuum permittivity, k_B the Boltzmann constant, e the electron charge, T_e the electron temperature and n_e the electron density.

Plasma frequency (ω_p)

In a thought experiment, an electrical field causes a displacement of electrons from ions in plasma. Immediately as the field is removed, the electrons are pulled back towards the ions. Owing to the high velocity of the electrons they are forced to oscillate about the ions with a certain frequency, called plasma frequency [9].

$$\omega_p = \sqrt{\frac{n_e \cdot e^2}{\varepsilon_0 \cdot m_e}},$$ (2.2)

where m_e is the electron mass.

2.2.2 Plasma reactions

Collision and reaction processes between the species are necessary to initiate and sustain the plasma and influence the entire plasma behaviour. Particles execute due to thermal fluctuation elastic and inelastic collisions. In elastic collisions the kinetic energy is exchanged, the potential energy of both particles is conserved. As a result no ionisation or excitation occurs. In contrast, at inelastic collisions also kinetic energy is exchanged nevertheless linked with a change in potential energy of the particles. A part of kinetic energy is used for ionisation or other excitation processes [6].

2.2.3 Plasma discharges

One way to generate a technical plasma is the application of a sufficiently high DC voltage between two metal electrodes. At low gas pressures and above critical electric field strengths free electrons, which are always present due to cosmic rays, etc., are accelerated towards the anode and ionise neutral gas particles at collisions. As a consequence more free electrons exist and ions are accelerated. For low applied power the number of charge carriers is small and the voltage is limited by the impedance of the power supply. This state is called Townsend discharge, shown in Figure 2.1. With further increasing current density the ionisation becomes avalanche-like above a certain threshold. In normal glow state the plasma is self-sustaining, which is accompanied by a voltage drop. Furthermore, the ion bombardment is concentrated on edges and irregularities of the cathode (target). An increase of current density causes ion bombardment over the entire target surface. This following state, called abnormal discharge,

is the operating zone for sputtering. Still higher current density causes target heating and as a consequence thermally emitted electrons together with low voltage arcs. In this state, cathodic arc evaporation starts, see Figure 2.1 [6].
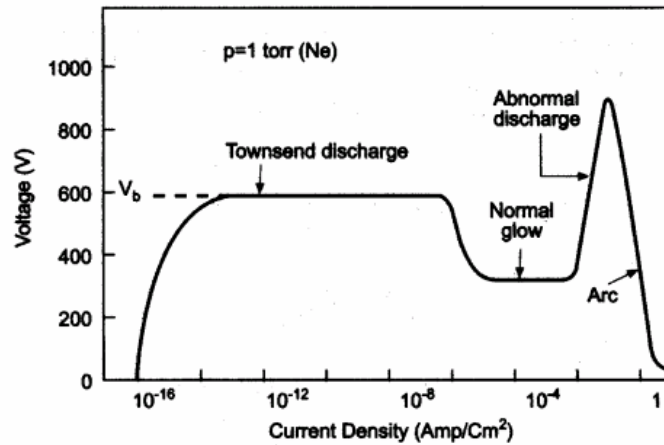
Figure 2.1: Voltage versus current density curve of a DC plasma discharge [10].

2.3 Cathodic arc evaporation

Basically, arcs are defined as high-current, low voltage gas discharges. As in common welding, to ignite the arc two metal electrodes are brought in contact first and then divided on short distance. Thus a very luminous and small cathode spot is formed which transfuses extremely high current densities ($\sim 10^8$ up to 10^{12} A/m^2). As a result, the cathode (target) material becomes molten and vaporised. Also the ejection of liquid and solid particles can be observed. These emitted particles are also called droplets. The arc is sustained by multivalent ions in the vapour. During this discharge the arc is moving rapidly on the surface in a random walk (closer description in chapter 2.3.3). Parameters influencing the direction of the arc are cathode composition, gas species, pressure and magnetic fields. Furthermore, external magnetic fields are the major parameter to influence the arc and by this also the film deposition. On the other side, at the anode, much smaller current densities are present ($\sim 10^5$ A/m^2), which can also cause erosion by evaporation and melting [6]. In cathodic arc deposition, the anode is merely a passive electron collector. For the case that the anode surface is very small or thermally insulated or the discharge current is very high, anode spots may also occur and cause evaporation [11].

A schematic illustration of a cathodic arc source is shown in Figure 2.2. Important details are the arc ignition mechanism, usually mechanical strikers are used, and the implementation to confine the arc on the targets surface. Several different concepts exist to confine an arc on the targets surface, e.g. by magnetic fields, by boundary shields, which extinguish the arc in case of contact or by passive borders, which surround the cathode and are made from insulating materials.

Next to the confinement of the arc, the magnet system has also other substantial functions. A uniform film deposition can be achieved by magnetically induced arc movement on the target, which cause a series of flash evaporations. As a result, desirable metal ions and neutrals are emitted and also undesirable droplets can be observed (detail illustration in Figure 2.2). Droplets are molten or solid cathode particles which are emitted due to thermal shock or other effects. The majority of the droplets are emitted in a low angle respective to the target surface. Hence, an effective way to reduce the droplets on the substrate is a low-angle shielding. Other possibilities for a droplet minimization are the reduction of the arc current, adjustment of process pressure or an increase of the arc spot velocity on the targets surface. Also a filtering of the emitted plasma with curved, electromagnetic mass filters is possible [6].
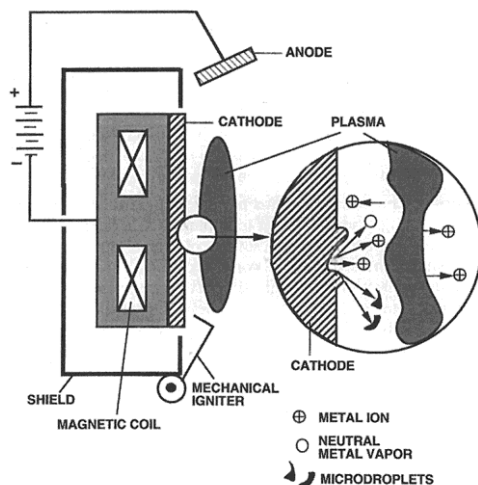
Figure 2.2: Schematic cross section of a cathodic arc source with a model of activity at a cathodic arc spot [12].
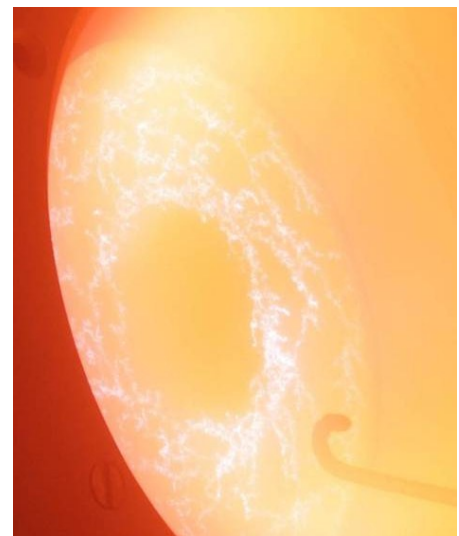
Figure 2.3: Cathodic arc source during film deposition [13].

2.3.1 Physical processes on the cathode

The very complex physical processes on the cathode are until today not understood completely and still subject of discussion. One of the basic questions is how the emission of electrons occurs. It is well known, that macroscopic electric current is made up of an electron motion in the conduction band of metals. For the case a plasma is present between anode and cathode a current built up from motion of charged particles flows between the two electrodes. Most of the current is transported by electrons because of their low mass and thereby high mobility compared to ions.

The important areas of current flow are the interfaces between metal and plasma. At the cathode, electrons in the conduction band have to hurdle a potential barrier, also called the work function of the cathode, to become emitted in a plasma. The effects leading to emission of electrons can be divided into two categories, first individual events and second collective

effects. An individual event e.g. is the impact of ions, whereas collective effects are the emission by high cathode temperature or high electric field on the cathodes surface.

The potential between cathode and anode is not evenly distributed. A schematic overview is shown in Figure 2.4. The potential drop close to cathodes surface is most significant for the emission of electrons by ion impact. These sheaths of the electrodes are in reality very thin. Also the descent representing the plasma resistance is exaggerated. On the anode, the drop can be positive or negative depending on different factors i.e. anode current, anode area and other factors [11].
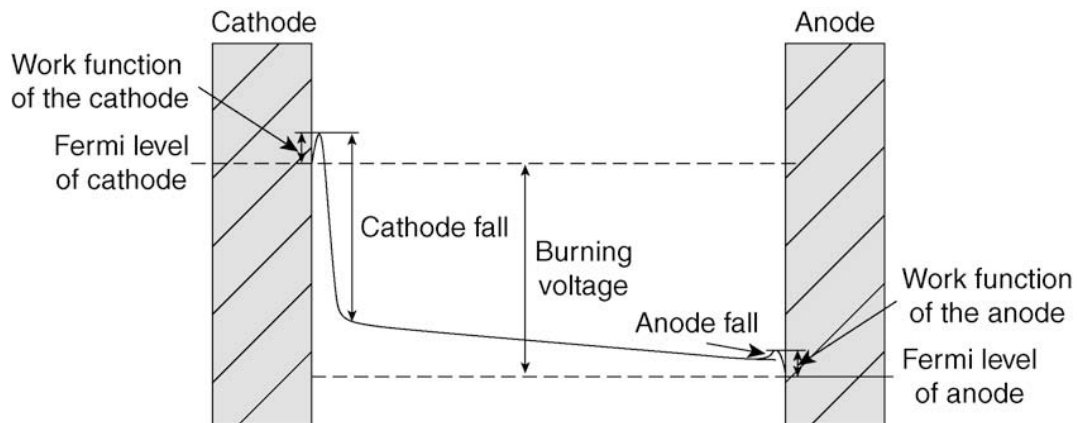
Figure 2.4: Schematic figure of the potential distribution between cathode and anode [14].

The cathode fall (the voltage drop close to the cathodes surface) is significant for the cathodes mechanism and necessary to maintain the discharge. In glow discharges, ions from the bulk plasma become accelerated by the cathode fall and strike on the target surface. By this effect, secondary electrons are emitted and also recombination of ions occurs. The voltage drop is usually in a region of 400-500 V, so secondary electrons have enough energy to heat plasma electrons and to cause ionization in the plasma. As a consequence the cathode fall is self-adjusting. In detail this means, if the electrons don't gain enough energy in the cathode sheath, the plasma generation will decrease and furthermore the plasma density decreases too. As a result the electrical resistance of the plasma increases and by this the burning voltage will increase. This means also an increase in voltage drop at the cathode and so also a higher energy of the secondary electrons. This correlation clarifies that secondary electrons are vital for the operation of the plasma discharges.

In contrast, in arc evaporation, secondary electrons cannot be emitted by ion impact. Therefore other collective mechanisms enable the emission of secondary electrons, thermionic emission and emission by strong electric fields [11].

2.3.2 Collective electron emission

Thermionic emission

The most accurate way to describe the thermionic emission behaviour of electrons is by Fermi-Dirac statistic. The Fermi distribution describes the probability that a state of energy is occupied at a certain temperature. The investigation of the Fermi distribution of metals at different temperatures shows that even at the melting temperature the majority of the electrons is still in low energy states [11].
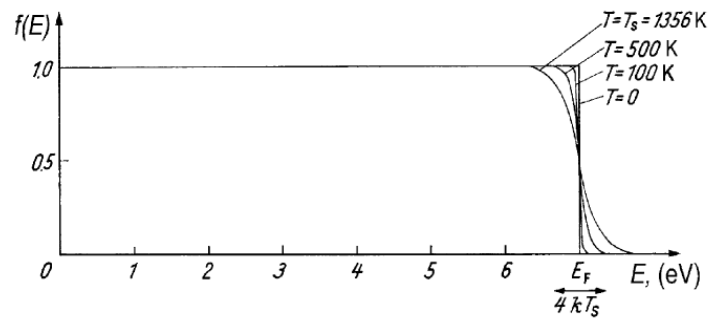
Figure 2.5: Fermi distribution function of Copper at different temperatures [11].

The emitted current density can be calculated according to the Richardson-Dushman equation, which is [11]:

$$j_{thermionic} = \frac{4\pi e m_e {k_B}^2}{h^3} \cdot T^2 \cdot \exp\left(-\frac{\phi}{k_B \cdot T}\right), \qquad (2.3)$$

where h is the Planck's constant, T is the temperature and ϕ is the work function.

Field emission

The previous part excluded the presence of electric fields, which influence the emission behaviour. In reality, an electric field is always present, even the emitted electrons located close to the surface cause a rearrangement of electrons in the conduction band. Hence, a closer look on field-enhanced emission is essential.

As mentioned above, an external electric field ($\mathscr{E}$) influences the potential barrier (ϕ), where an electron has to hurdle to become emitted. By superposition of both potential distributions a reduction in the maximum height of the potential barrier can be shown. As a result of this classical physical interpretation a higher emission can be observed.

However, the situation changes in the case that very strong electric fields are applied on the cathode. Quantum mechanics are necessary for this description. The shape of the potential barrier becomes deformed by the external electric field. The reduction in height and width of the potential barrier enables electrons-tunnelling through the barrier. The different shapes of potential barriers can be seen in Figure 2.6. For calculation of the tunnelling probability it is

necessary to solve the Schrödinger equation three times (inside the metal, inside the barrier and outside the metal and the barrier) [11].
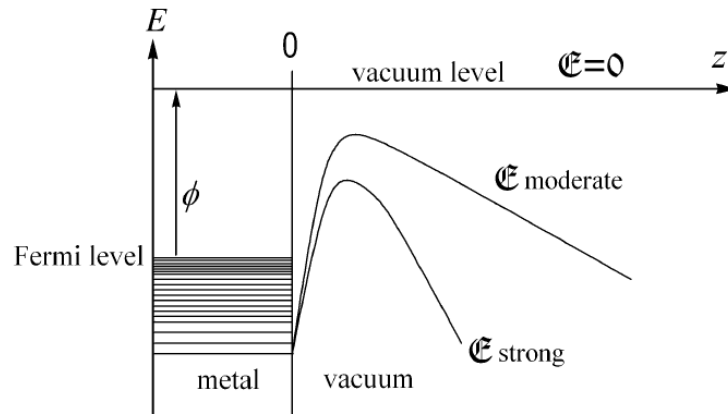
Figure 2.6: Potential barrier of a metal surface at different electric field strengths [11].

2.3.3 Explosive electron emission

Until now, no mentioned model describes the influence of time on the emission process. Considering the energy balance on an emission spot the situation changes, due to two major processes. First, the ion bombardment from the plasma and second, the resistive heating of the cathode emission current cause a temperature enhancement. Cooling occurs owing to heat conduction, radiation and electron emission. Generally heating and cooling are not in balance. As a result, the temperature becomes a time dependent variable. In the case of a high electric field and the emission is already on a high level, a positive result can be obtained. In detail, the heating of emission current leads to a local higher temperature, which accelerates the emission further. The higher emission leads to a higher local emission current and further on. Such a development can lead to a localized evaporation in an explosive manner. This form of electron emission is also called explosive electron emission.

It is obvious that the explosive electron emission is a non-stationary process, whereby also a plasma of the emitted material is generated. During emission not only electrons are emitted, but also ions and neutrals of the target material. Depending on the target material a specific energy is necessary to explode or ignite an emission centre [14].

The emission cycle proceeds in four highly dynamic stages: (1) the pre-explosion stage; (2) the explosive emission stage; (3) the immediate post-explosion stage; and (4) the final cool-down stage. The term "ignition" means in this context the perpetual and repetitive mechanism of the arc discharge for a macroscopic continuous discharge.

(1) The pre-explosion stage

At the target surface exists more and less favourable positions for an ignition of an emission centre. Depending on the local work function, geometric conditions, surface coverage by oxides or other insulators, etc. a local higher energy input than at other locations can occur. A low local work function, a high electric field due to micro-protrusions and a high intensity of ion bombardment can lead to the origin of an emission centre and hence transfer the location in stage 2 [14].

(2) The explosive emission stage

The key element of this stage is the thermal runaway, whereby the electron emission and the heating by emission current built an amplifying feedback loop. The micro-explosion causes erosion of a micro-volume. As a result a micro-crater is burst into the target surface [15,16]. Detailed investigations have shown the explosive emission stage takes a duration of 10-20 ns [17].

(3) The immediate post-explosion stage

In the freshly formed crater, most likely a surface layer of molten target material exists. Also the plasma at this spot is very dense, which facilitates a field-enhanced thermionic electron emission. Furthermore, evaporation of the liquid target material occurs. The material vapour has low conductivity, which stalls the electric current flow. This behaviour is also one of several reasons for the unsteady spot motion. The reasons therefore are discussed later.

In this stage also the plasma pressure impinges on the liquid material. This leads to the generation of microscopic droplets [14].

(4) The final cool down

Finally, the thermal conduction at the emission centre increases, so the hot area increases too. A temperature reduction is the consequence and analogically electron emission is reduced exponentially, see equation (2.3). Furthermore, the formed plasma has expanded, the sheath thickness has increased and also the electric field is lowered. An important aspect in this stage is the vaporization of a target hot material, especially if the material has a high vapour pressure [14].

As mentioned before, there are several reasons for the unsteady emission and the arc motion during evaporation. First, as mentioned in the paragraph before, heat conduction increases the size of the emission spot, and consequently the energy density in the spot is decreasing.

Second, also the electrical conductivity of the material changes with increasing temperature. For metals, the conductivity at high temperatures is lower, so areas with better conductivity exist in the close vicinity. As a consequence the current will switch to paths with higher conductivity.

Third, already mentioned before, in all states of matter of the target material, the gaseous state is the least conductive. Hence, the metal vapour in vicinity of the emission centre stalls the flow of electricity. Furthermore, as the size of the emission centre increases, the energy density and also the temperature of the emission spot decreases. Hence, the electron emission drops. In this moment, the plasma composition changes due to the neutral material vapour and influences the current additionally.

Fourth, in this situation the plasma has probably started a new emission on a spot with better conditions for emission [14].

Arc motion

Without external magnetic fields, the direction of the arc motion is evenly distributed. This means that the arc moves in a random walk above the target surface. Indeed, in industrial applications also a low surface roughness is favourable. The size of droplets on the coating correlates with the arc velocity, e.g. a slow arc produces a low number of big droplets and vice versa. Therefore the arc is steered by external magnetic fields. This means the arc is steered by the Amperian force in $j \times B$, with resulting motion in anti-Amperian direction [11].

2.4 Morphology of thin films

2.4.1 Nucleation and growth

Material properties of hard coatings are strongly dependent on the parameters of deposition processes. One reason therefore is that the synthesis of coatings occurs in the heavily thermodynamic disequilibrium. Atoms can become absorbed on the substrate surface or reevaporated, depending on beneath other parameter, their impinging energy. In Figure 2.7 the different reactions of arrived atoms are shown. Crucial for the formation of a coating on a substrate are the combination of atoms to clusters and the formation of nuclei. Following atoms accumulate preferentially on existing nuclei, which leads to an enlargement and further to the growth of a coating on substrate. The initial stage acts as a blueprint for the growing coating. Thereof, properties of the growing coating are strongly influenced.
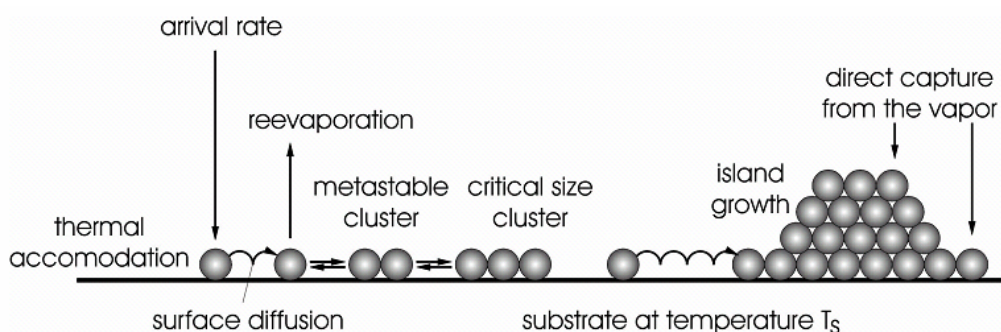
Figure 2.7: Schematic illustration of surface reactions leading to nucleation and crystal growth [18].

The following paragraph gives a rough overview about nucleation and growth of coatings [6,19].

1. Adsorption of atoms
2. Formation of highly mobile clusters or islands
3. Growth of clusters by impinging atoms and simultaneous a rapid increase in island density
4. Merging of islands by coalescence, especially at high substrate temperatures this phenomenon can be observed. Strong driving forces, like the reduction of surface energy are responsible therefore. Smaller islands assume the crystal orientation of the occupying ones. Due to coalescence the island density decreases and exposes fresh substrate areas.
5. Formation of clusters on the fresh substrate areas.
6. Coalescence leads to formation of a connected network with non-deposited channels between.
7. Further deposition shrinks the non-deposited areas and leads to the formation of isolated voids.
8. Finally all voids are covered, a continuous layer is built.

The real behaviour of material pairings in nucleation processes are described in three growth models, see Figure 2.8. The island (or Volmer-Weber) model describes a growth of the smallest stable clusters in three dimensions. This happens due to a stronger bonding between the deposited atoms than to the substrate atoms (e.g. metals or semiconductors on oxide substrates). The opposite behaviour is described by the layer (or Frank-van der Merwe) model. Thereby the nucleus extends in two dimensions, due to a higher attraction between the coating atoms and the substrate atoms. This leads to a layered structure and further a strongly bonded first layer. Following layers have lower bonding forces (e.g. single-crystal epitaxial growth of semiconductors). The Stranski-Krastanov is the intermediate model, between these two extreme cases. After formation of the first monolayers, the growth changes into the island model (e.g. metal-metal and metal-semiconductors systems) [6,20].
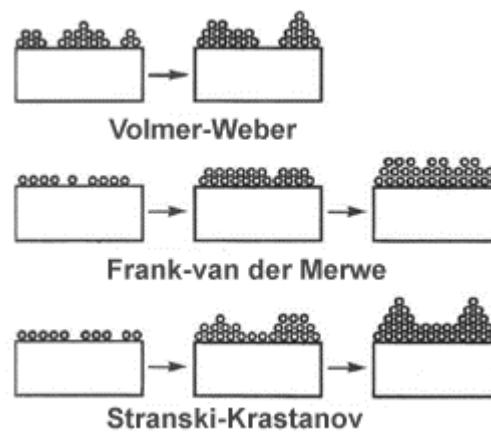
Figure 2.8: The three basic models of film growth [6].

2.4.2 Structure zone models

As mentioned before, the nucleation is important for the coating structure and properties. However, there are also other mechanisms proceeding during deposition, which influence the final structure and thereby also their properties. In detail, there exist four basic processes effecting the structure development; shadowing, surface diffusion, bulk diffusion and desorption. Shadowing means the interplay between impinging atoms and surface topography. The other three processes are connected with material constants, e.g. energies for diffusion and sublimation. These energies can be correlated with the materials melting temperature [6].

In industrial application it is necessary to forecast the final structure as a function of deposition process parameters. Therefore, in several investigations a structure zone model (SZM) has been developed. Movchan and Demchishin investigated the coatings microstructure and postulated the first SZM with three main zones, depending on the ratio of melting (T_M) and substrate (T_S) temperature [21]. The key variable of their SZM, and any following, is the homologous temperature (T_S/T_M). Thornton refined the SZM after broad investigations with an additional fourth zone, called transition zone, or T zone. Furthermore, the gas pressure was introduced as an additional parameter. Therefore, the SZM takes care of the decreasing energy of arriving atoms with increasing gas pressure, which results in a widened zone 1 due to a higher number of collisions [22].

The following paragraph gives a brief overview about the different zones in SZM's, which are displayed in Figure 2.9. More detailed information can be found in [5,6,21,22].

– Zone 1 is characterized by a limited atom motion on the surface. This results in a fine grained structure with a high imperfection density and porous grain boundaries. Zone 1 grains tendentially grow in the direction of the coating flux and is also strongly influenced by shadowing effects.

- Zone T has a dense fibrous structure without porous grain boundaries. Coatings of zone T have also a smoother surface morphology than the neighbouring zones. The widening of zone T with decreasing gas pressure is related with the more intense ion bombardment.
- Zone 2 consists of a uniform columnar structure with increasing grain sizes at higher temperatures. The structure is dominated by high surface diffusion and the surface has a mat appearance due to a highly faceted top.
- Zone 3 exhibits a coarse columnar structure. At highest temperatures due to bulk diffusion, an equiaxed recrystallized structure is formed.
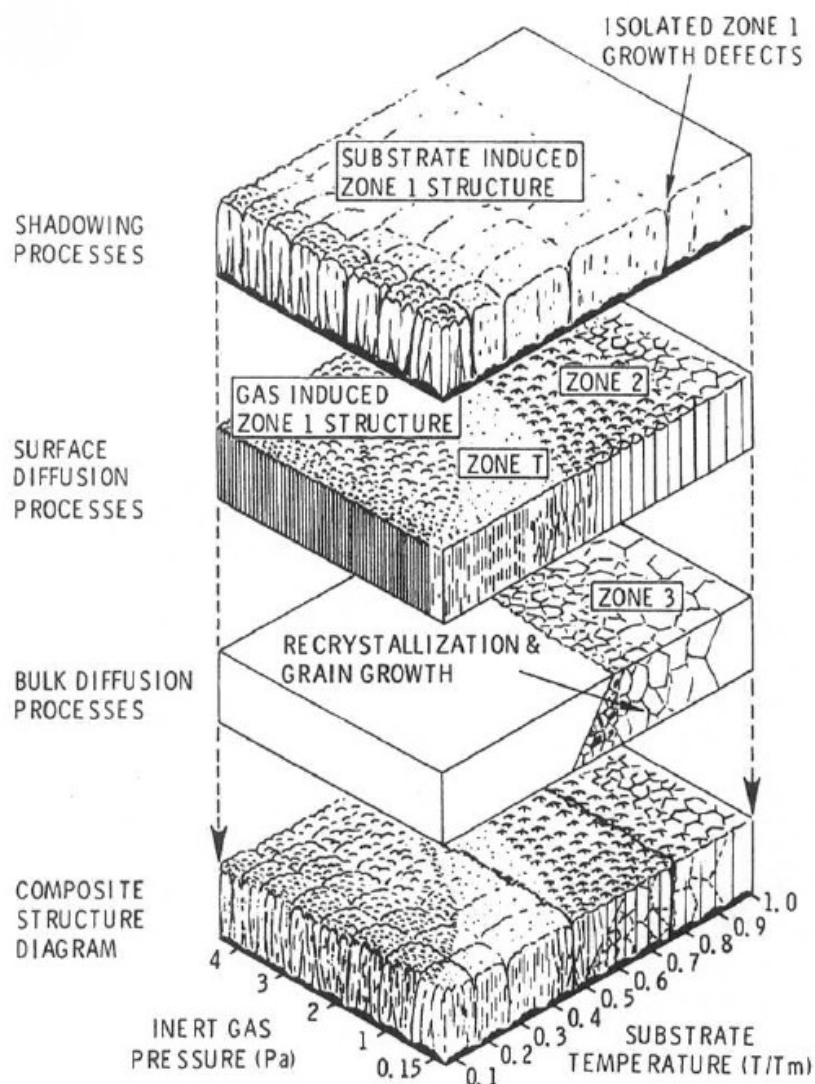
Figure 2.9: SZM of Thornton with a detached view on the influencing processes [6].

The effect of ion bombardment on coatings structure was investigated by Messier et al. (see Figure 2.10). Thereby the gas pressure was replaced by substrate bias voltage. The effect on SZM is, that zone T becomes inverted due to more intense ion bombardment at higher bias voltage (a comparable effect has a reduced gas pressure) [6]. Further results showed, that inside the zone 1 and T, the intrinsic structure can be polycrystalline or amorphous [5].
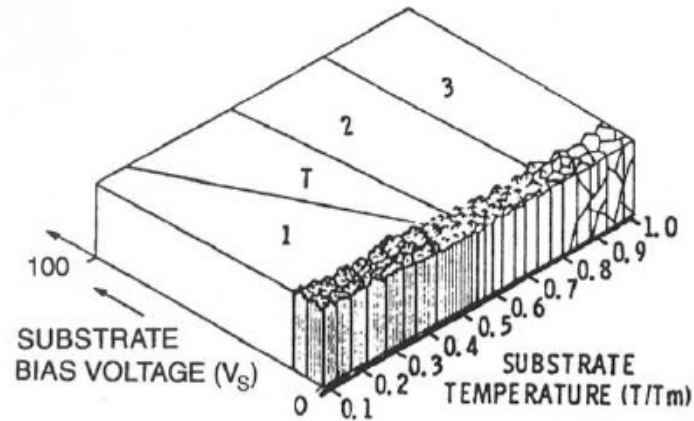
Figure 2.10: SZM of film growth, illustrating the influence of ion bombardment [23].

3 Experimental

3.1 Deposition

3.1.1 Deposition system INNOVA

The hard coatings were developed on an Oerlikon Balzers INNOVA deposition plant, displayed in Figure 3.1. This is an industrial deposition plant with up to six sources for arc evaporation. The process chamber volume is ~1 m^3. The arc sources are vertically mounted on 2 height levels and have a target diameter of 150 mm. The carousel has 10 trees and each tree executes a 2 fold rotation during the whole process. The distance between sources and substrate is ~235 mm.

As already mentioned, the magnet system of the target has a major influence on the evaporation characteristic and also on the coating properties. The magnet system in use has the code MAG6 and consists of a coil inducing a magnetic field up to 2 mT at a coil current of 1 A. The even erosion behaviour is one characteristic of this magnet system, compared to others.
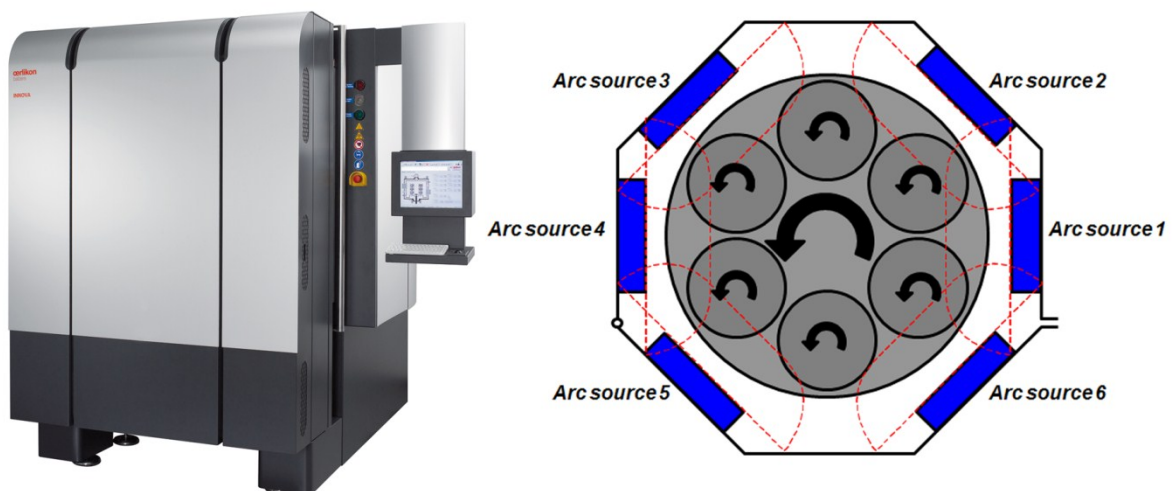
Figure 3.1: Left, picture of the INNOVA coating machine [13]. Right, schema of the deposition chamber with the configuration of the arc sources [24]

3.1.2 Deposition procedure

All deposition batches were done in the same scheme. The process starts with evacuation of the process chamber, followed by heating up to 480 °C. The heating step was supported by a plasma generated by a low voltage arc in the centre of the chamber. The plasma was built up of a mixture of Argon and Hydrogen. After heating, the etching step started. Etching was

done also with central arc and supported by a bias voltage applied on the substrates. With finishing of etching, the coating deposition started. With respect to the different number of operating sources the deposition time was adopted to reach a coating thickness of approximately 5 μm (e.g. deposition time in run #10 was 90 min). Further details to deposition parameters can be seen in the following chapter.

3.1.3 Deposition parameters

In Table 2 the major deposition parameters are displayed.

Table 2: Overview of most important deposition parameters

Arc current [A]	Coil current [A]	Pressure [Pa]	N_2 ratio [%]	Bias voltage [V]	Substrate rotation [min-1]	Magnet system
150	0.6	2	100	-40	1.58	MAG6

For the coating development different substrates were used and analysed (see Table 3). In all deposition batches, the substrates were fixed with magnets onto the carousels tree.

Table 3: Overview about the used substrates, their materials and geometry

Code	DIN Number	Material	Geometry
QRS	1.2842	90MnCrV8	Ø 22 x 5.6 mm
SDK	1.3343	S652	Ø 15 x 3.5 mm
THM	-	WC with 6% Co	12 x 12 x 3.18 mm
SMS	1.3343	S652	Ø 29 x 0.5 mm
SRV pin	1.2379	X155CrVMo12-1	Ø 10 x 10 mm
Drawing jaws	-	Cr7V	18 x 14.8 x 60 mm

It was not possible to realise every coating composition from the available targets. By this reason different target compositions were used in the deposition batches. For this, a denser variation of chemical composition could be achieved. The three available target compositions had a Si content of 5, 10 and 20 at%. In addition pure Chromium targets were used. All Cr/Si targets were produced by powder metallurgical way. The target arrangement of the different deposition batches is given in Table 4. The deposition run #10 has the speciality of homogenous target chemistry, different to all other runs. In respect to this speciality the coating has the suffix "STC", which stands for same target chemistry. The resulting chemical composition of the coating is shown in chapter 4.2.

Table 4: Target configuration of all deposition batches.

	Arc sources						
Run	1	2	3	4	5	6	Si_{th}
#1	Cr	Cr	Cr	Cr	off	off	0.0
#2	Cr	Cr	Cr	Cr	90/10	90/10	3.3
#3	Cr	off	off	Cr	90/10	90/10	5.0
#4	Cr	Cr	Cr	Cr	80/20	80/20	6.7
#5	Cr	95/5	95/5	Cr	80/20	80/20	8.3
#6	Cr	off	off	Cr	80/20	80/20	10.0
#7	95/5	off	off	95/5	80/20	80/20	12.5
#8	90/10	off	off	90/10	80/20	80/20	15.0
#9	off	off	off	off	80/20	80/20	20.0
#10	95/5	95/5	95/5	95/5	95/5	95/5	5.0
-	The numbers represent the chemical target composition of Cr/Si in at%						-

3.2 Methods of coating characterization

For an entire imagination of the coating properties several different analysing methods were used. Only a short explanation will be given to the standard characterization methods like thickness measurements, adhesion testing.

Thickness measurement

The coatings thickness was measured by the calotte grinding method. For this, a tungsten carbide ball in combination with a diamond suspension of 1 µm was used. The grinding speed varied between the measurements. All calottes were grinded on a CSM Calotest industrial, the final diameter measurement was done on an Olympus MX40 microscope. An approximation for thickness determination is,

$$t_c = \frac{D_0^2 - D_i^2}{4 \cdot D}$$

(3.1)

Adhesion testing

For comparison of the adhesion behaviour Rockwell C indentation on QRS substrates was done. The evaluation of the adhesion was done according to the standard VDI 3198. The characterisation schema of the HRC indents is displayed in Figure 3.2.
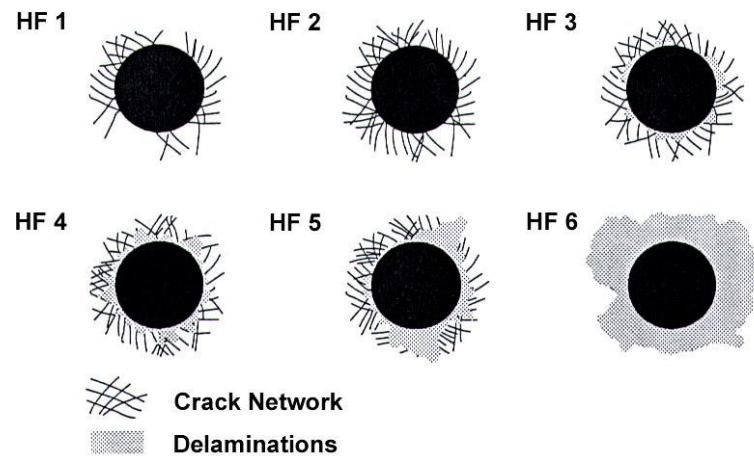
Figure 3.2: Characterisation classes of film adhesion in the Rockwell C test [25].

Wear measurements

The determination of the wear behaviour was done by two different methods. First, the wear coefficient was measured by the calotte grinding method. The used analysis device was a BAQ kaloMAX NT. Thereby a calotte was grinded in the coatings surface at defined environment conditions. Constant measurement parameters were: normal load, sliding speed and time, amount of suspension. The allowed range for relative humidity was from 37 % to 43 %. The diameter of each grinded calotte was measured three times and an average diameter was calculated. Each measurement consisted of three calottes. The relative wear coefficient results from the average diameter of these three measurements. This interim result was still influenced by environment conditions like temperature and humidity. These influences were minimized by comparison with a reference sample.
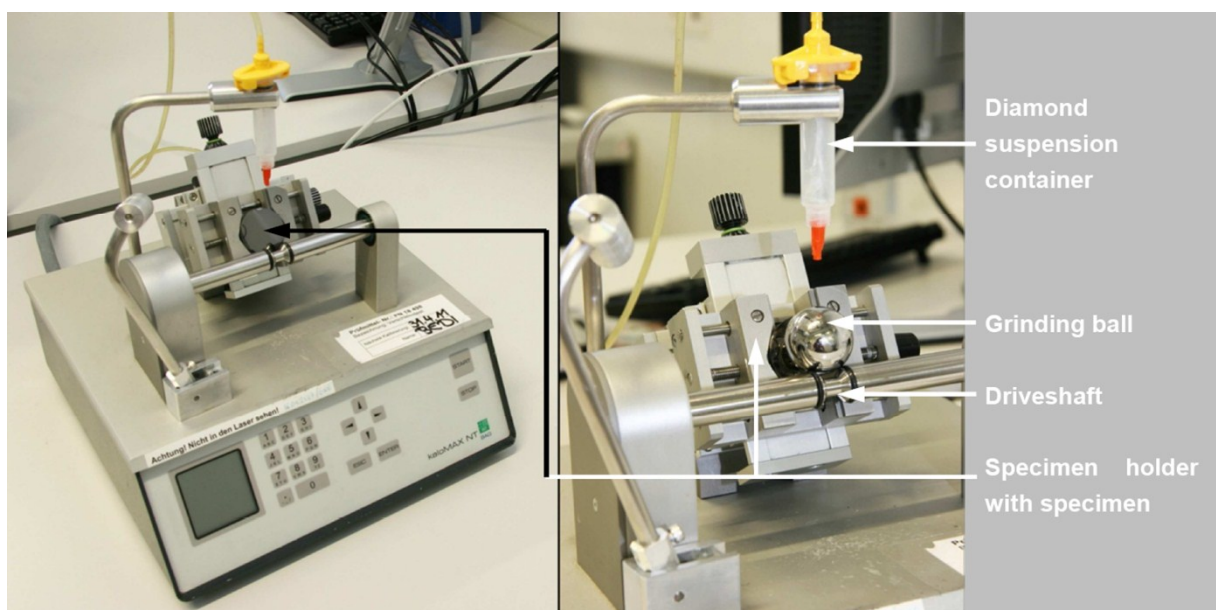
Figure 3.3: Measuring instrument for determination of wear coefficient.

The second procedure to measure the wear coefficient was the analysis of a ball on disk wear track by scanning white light interferometry. The used model was a nanofocus µsurf[®].

In the interferometer a beam from white light is generated and split into separated beams. One becomes reflected on the samples surface, the other becomes reflected on a highly smooth reference mirror. The two reflected light beams recombine in the interferometer and if the sample is focus, a characteristic interference pattern of bright and dark lines is formed. The interference pattern is detected with a CCD camera and the software calculates the 3-dimensional profile. The software also determined the negative volume in the wear track, what from a wear coefficient was calculated [26].

3.2.1 Micro-Indentation

Hardness and Young's modulus are two major material parameters in material science. Usually hardness is defined as the mechanical resistance against deformation. A more practical definition of hardness is the ratio of peak load F_{max} and the residual projected indentation area A_p.

$$H_{IT} = \frac{F_{max}}{A_p}$$

(3.2)

In case of bulk materials the evaluation of the residual projected indentation area occurs optically after indentation. Caused by the low material thickness in coating technology it is essential to ensure that the measured parameters are not influenced by the substrate. For this it is necessary to limit the maximum indentation depth to 10 % of coatings thickness, this limitation is also called Bückle rule [27]. Through adaption of the indentation force this limitation can be insured. Instrumented indentation means further that during measurement continuously the normal force and indentation depth is recorded. This load displacement curves are characteristic for materials and material properties e.g. hardness and Young's modulus. Both parameters were calculated using the Oliver-Pharr method [28].

In detail all measurements were done with a FISCHERSCOPE[®] HM100C, the indenter was a Vickers diamond. An illustration of an indentation is displayed in Figure 3.4 (a) and also a typical load displacement curve, see Figure 3.4 (b).

h_{max}	Total indentations depth measured from specimen free surface
h_r	Depth of residual impressions
h_e	Elastic depth of penetration for unloading
h_c	Depth of the contact indenter - material
A_c	Contact area under peak load
F	Indentation Force
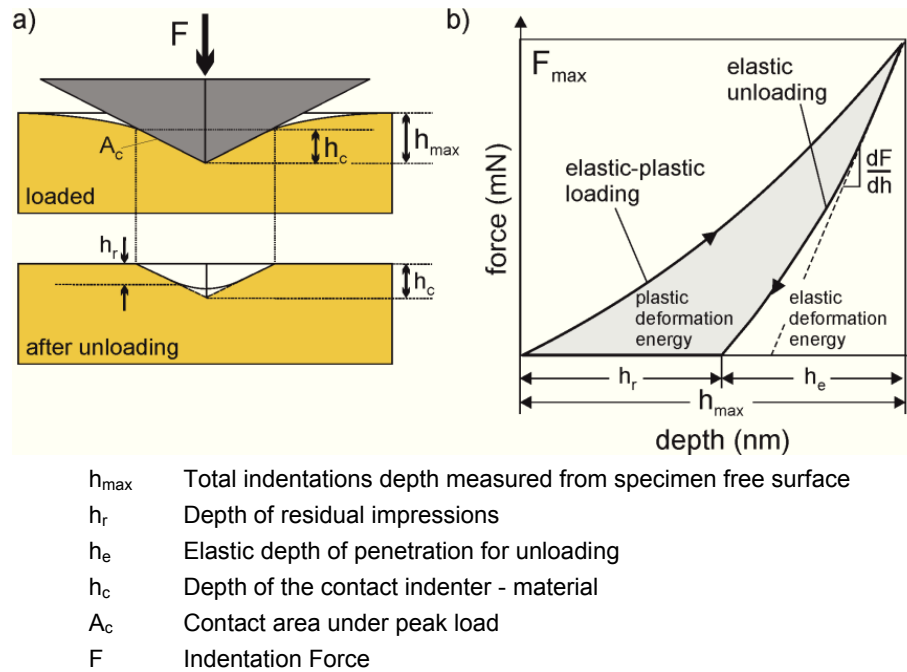
Figure 3.4: Schematic illustration of an indentation at full load and full unload for an elastic-plastic indentation (a); Load displacement curve in a typical hardness measurement (b) [29].

To exclude the potential influence of surface roughness and impurities, the sample was polished with a steel ball before testing. The polishing was done without suspension for 10 seconds. After a check of the calotte's depth the hardness measurements were performed within this crater.

3.2.2 X-ray diffraction (XRD)

X-ray diffraction (XRD) analysis is a non-destructive characterisation method for crystalline materials. Moreover, structural properties like grain size, texture, residual stresses and phase changes can be analysed.

The basic physical principle behind this technique is the reflection of electromagnetic waves on certain lattice planes. When the wavelength of the electromagnetic waves is in the order of a magnitude of the crystals lattice plane parameter, a characteristic diffraction pattern is generated. The correlation of the diffraction angle θ with the lattice plane distance d_{hkl}, h, k and l represent the Miller Indices, and the wavelength λ of the used radiation is called Bragg's law and can be written as [30],

$$n \cdot \lambda = 2d \cdot \sin(\theta). \tag{3.3}$$

A schematic illustration of Bragg's law is displayed in Figure 3.5. Furthermore, the measurement setup for XRD measurements is can be seen in Figure 3.6.

Figure 3.5: Schematic illustration of X-ray diffraction on atomic lattice planes [31].

Figure 3.6: Setup for XRD measurements [20].

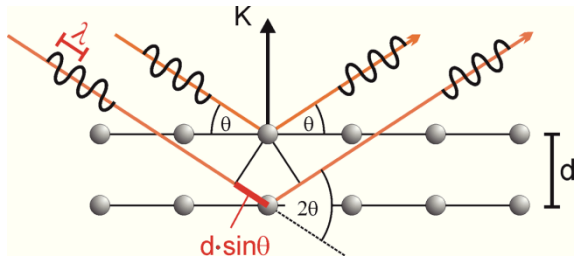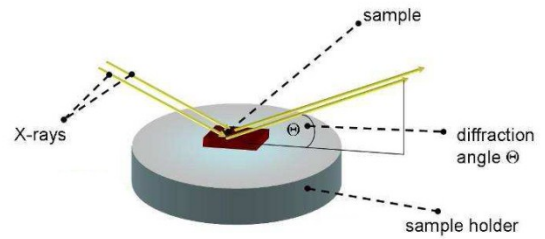Through comparison of the measured diffraction pattern with the peak positions and the relative intensities of standard patterns phase analyses can be done. In this thesis standards of the International Centre of Diffraction Data (ICDD) were used.

X-ray diffraction offers several different measurement setups. In this work the Bragg/Brentano and the detector scan (also called glancing incident measurement) setups were used. For all measurements a Bruker AXS D8 advanced diffractometer with a SolX detector was used. At Bragg/Brentano setup the sample surface is irradiated under the angle θ and the diffracted beam is collected by the detector under the angle 2θ relative to the incident beam. At the used setup, the samples position was fixed, hence tube and detector moved with the same speed and angle relative to the sample surface.

For surface sensitive measurements the detector scan setup was used. Therefore, the angle of incident beam is fixed, in this thesis the angle was 3°, and diffracted beams were collected by the detector in the same way as during Bragg/Brentano setup.

Residual stress measurements can be done in different arrangements. Due to the opportunities on the diffractometer, the ω-mode was one possibility to measure the residual stresses by XRD. A detailed description of residual stress analysis can be seen in [32]. In this thesis all measurements were done on the (422) peak. For Cr-Si-N coatings, the "roentgenographic" constants of CrN were used; all used parameters can be seen in Table 5. These simplifications will influence the absolute residual stress values, but not the trend and the relations between the different samples.

Table 5: Used roentgenographic constants for residual stress calculation.

coating	S_1 [TPa^{-1}]	$\frac{1}{2}S_2$ [TPa^{-1}]
Cr-N and Cr-Si-N	-0.77	3.98
LUMENA	-0.711	3.569
ALCRONA Pro	-0.625	2.708

Additional to these results the lattice parameters were calculated. Basis for these calculations was the strain free lattice spacing of the (422) peak, which has already determined during residual stress evaluation. The determination of the strain free lattice spacing is discussed in detail in [32].

Another investigation, which was done on XRD measurements, is the determination of grain size. Therefore the three most significant peaks were used ((111), (200), and (220)) to calculate the grain size from full with of half maximum by using the Scherrer's formula. Further information can be seen in [33].
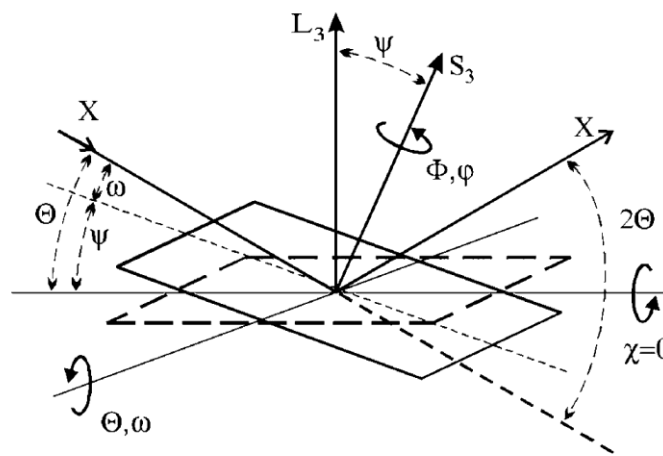
Figure 3.7: Definition of the various angles during residual stress measurements using the ω mode (L3 is the diffraction vector, S3 is the surface normal) [32].

Table 6: Parameter of XRD measurements

Wavelength [Å]	Tube voltage [kV]	Tube current [mA]	Step size [°]	Step time [s]
1.54060 (Cu K_α)	40	40	0.02	2

3.2.3 Oscillation-wear tester

The oscillation- wear tester (see Figure 3.8) offers the possibility to compare results from friction and wear experiments with application-oriented hardware simulations. The used machine is an OPTIMOL® SRV (Schwingung, Reibung, Verschleiß) with a heated lower specimen holder, which allows temperatures up to 900 °C. In this setup an upper specimen was moved with an electromagnetic drive against a lower stationary specimen. The load between the upper and lower specimen was generated by an arrangement of a spring and a servomotor. The heating cartridge is mounted in the lower specimen holder, underneath the lower specimen. The detection of friction force happens by two piezoelectric transducer

mounted at the lower specimen holder. The control and data acquisition during the experiment took place by a special PC program.
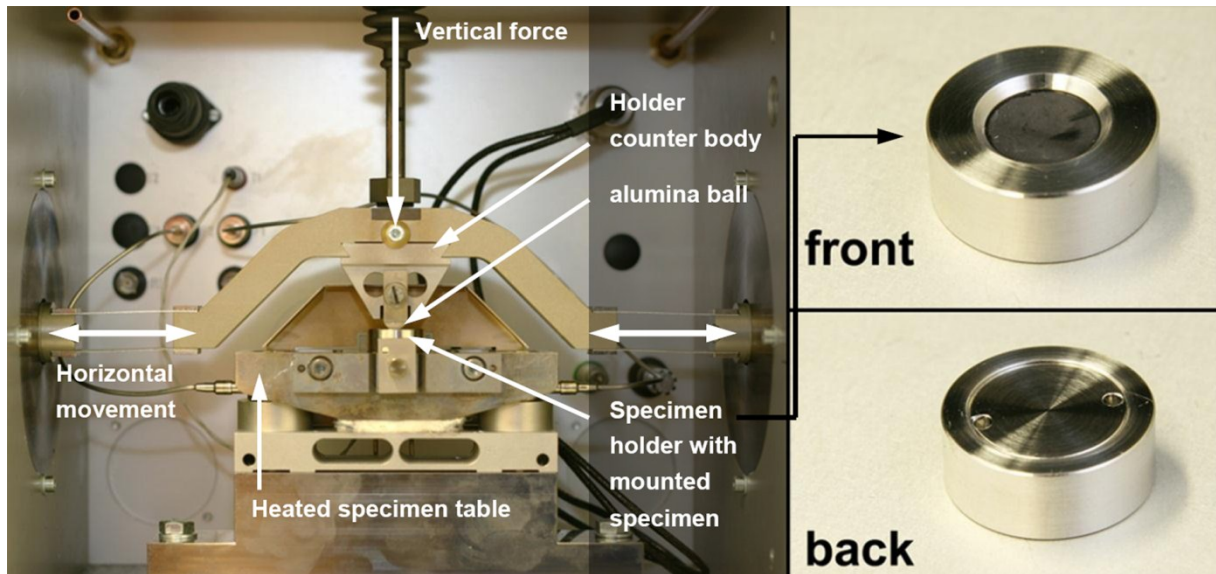
Figure 3.8: Left, picture of SRV tester and right, sample holder with mounted sample inside

In case of friction and wear experiments, the friction partner was an alumina ball with a diameter of 10 mm. For adhesive wear testing, a coated pin was moved against a heated USIBOR[®] 1500 steel sheet. For both setups a specimen adapter was necessary to achieve the correct specimen height [34].

Table 7: Testing parameters for wear measurements on SRV tester

Vertical force [N]	Stroke length [mm]	Frequency [Hz]	Testing time [min]	Temperature [°C]
10	1	5	10	25 and 800

Table 8: Testing parameters for Pin on USIBOR[®] tests on SRV tester.

Vertical force [N]	Stroke length [mm]	Frequency [Hz]	Testing time [min]	Temperature [°C]
10	4	1	2.5	900

The vertical force has to be above a threshold of 5 N due to a lower limitation by the friction force detectors. Therefore, the vertical force was set to 10 N.

In concert with hardware tests, measurements were done to determine the inclination for adhesive wear of the different coatings. Therefore, the alumina ball was replaced by the coated SRV pin, which was moved against a heated USIBOR[®] steel sheet.

3.2.4 Hardware simulation

For simulation of the complex demand spectra in press hardening a very specific test has been used. At this hardware simulation a heated aluminium-silicon coated steel sheet (USIBOR® 1500, 22MnB5, geometry: 500 mm x 50 mm x 1.5 mm) is drawn through two jaws. The steel sheet is heated up in an electrical conveyor belt oven up to 930 °C. The steel sheet stays for 390 seconds in the oven. After heating, the steel sheet is forwarded automatically to the drawing platform. In the following hot-forming device, two drawing jaws are pressed against the steel sheet with a normal force of 3 kN, while this is drawn through with a constant speed of 60 mm/s. An illustration of the measurement setup is displayed in Figure 3.9. During the drawing procedure the shear force and the drawing force is measured. Out of that, the friction coefficient µ can be calculated.

$$\mu = \frac{F_{draw}}{2 \cdot F_{shear}} \tag{3.4}$$

Each pair of drawing jaws was claimed five times. Additional to the measurement of the forces the drawing jaws were photographed and the smeared areas size determined. All these measurements were done at METAKUS GmbH, Baunatal, Germany [35].
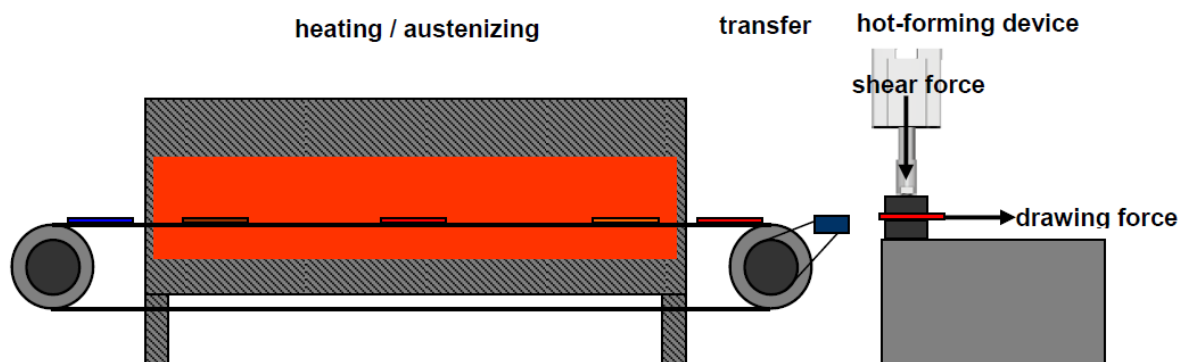
Figure 3.9: Illustration of measurement plant of hardware tests to determine the adhesive wear behaviour [35].

3.2.5 Scanning electron microscope (SEM)

Surface structure analysis and cross section investigation were done on a Zeiss LEO 1530 Gemini field emission scanning electron microscope (SEM). The chemical analysis was done with a fixed EDAX Leo 1530 energy dispersive x-ray spectroscopy analysis gadget. Furthermore a K. E. Developments Centaurus detector was used for back scattered electrons (BSE) investigations. Additional to the calotte grinding method, the thickness was also measured by SEM at cross section investigations.

3.2.6 Substrate treatment

Pre treatment

All substrates were cleaned before they were coated. The cleaning happened in the industrial cleaning plant USI 2000. Thereby the substrates move alternately into ultrasonic cleaners with alkaline detergents and deionised water. After the first 4 cleaning steps, the substrates become intensively swilled with deionized water. Afterwards, in two drying steps with temperatures up to 130 °C, the water is removed again. In this stadium the substrates are stored and ready for deposition. Before the deposition the substrate were cleaned one last time with a tissue and Isopropanol to remove loose particles from the surface.

Post treatment

The surface roughness of the coatings in as deposited state is not on an applicable level due to droplets. Therefore the coatings were polished after deposition. First step of post treatment, the coatings are grinded with 3M Scotch Bride™, very fine. Surface finishing was implemented by polishing the coating with a 3 μm diamond paste on a flannel disk. This procedure is in concert with the preparation for industrial application.

4 Results and discussion

An important part in press hardening of USIBOR[®] steel sheet is the texture and structure of the coating on the steel sheet. Therefore, SEM cross section investigations were done on steel sheets before and after hardware simulation. A brief overview about the results of this investigation is given in the following chapter 4.1.

4.1 Characterisation of steel sheets coating

The steel sheets coating consists basically of the elements Al, Si, Fe, and C. These elements are inhomogeneously spread about the coating thickness of approximately 7 μm, see Figure 4.1. The rough surface is enriched with Al, Si and Oxygen. In the interface between coating and steel the Al content is lowered, compared to the middle of the coating, whereby the Si and Fe are present in higher concentrations. Between these two interfaces a Si depleted region exists. This initial dispersion changes during the heating for press hardening. Due to heating for press hardening process, the top layer is Al enriched followed by a broad Si enriched layer. The Si depleted zone in the middle is even wider than at the initial state. The interface between steel and coating is sharpened by a significant Si peak and furthermore, Si diffusion in the steel sheet is measureable.
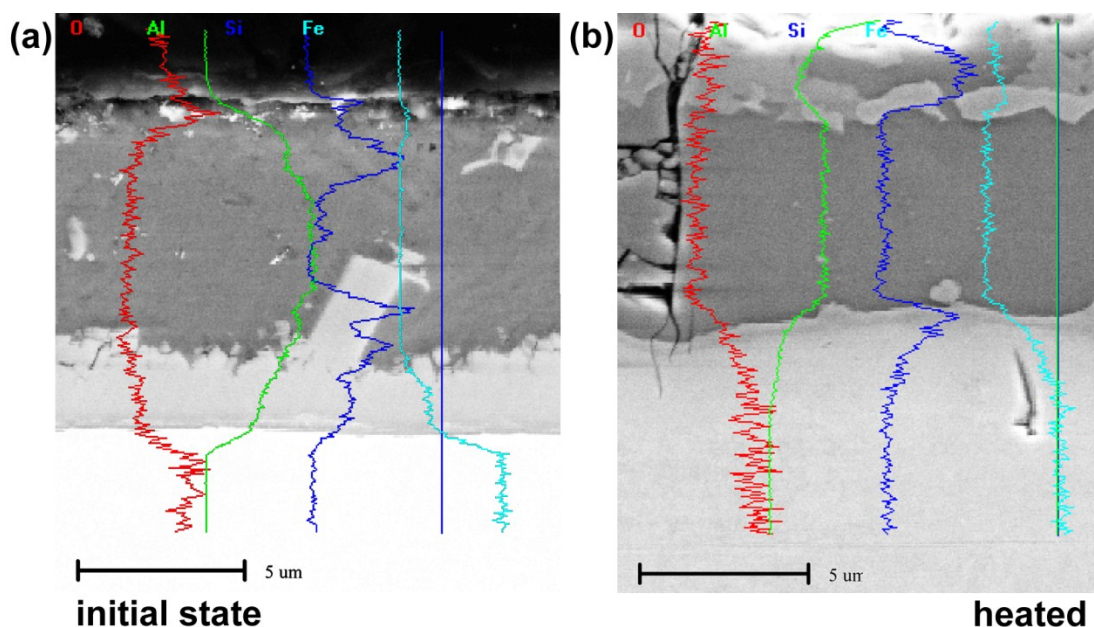

Figure 4.1: EDX line scans of USIBOR[®] steel sheets before (a) and after (b) a hardware test.

4.2 Chemical composition

As already mentioned in chapter 3.1.3, the deposition batches were conducted with targets having different Si contents. The final chemical composition of the coatings was detected by EDX measurements on QRS substrates. These measurements were done at a magnification of 1000, the working distance was 15 mm and the acceleration voltage was 15 kV. Before depositions, a theoretical Silicon content Si_{th} was calculated by the average chemical composition of all targets used. Table 9 contains the determined chemical composition of the coating in the form of $Cr_{1-x}Si_xN$; the Nitrogen content in the coatings was 55±3 at%.

Table 9: Chemical composition is shown of coatings in as deposited state, measured by EDX. The Nitrogen of all coatings was 55±3 at%, hence stoichiometric nitrides. Thus, the Cr and Si contents were normalized to 100 %.

	Deposition run									
	#1	#2	#3	#4	#5	#6	#7	#8	#9	#10
Cr	100.00	97.0	95.7	94.2	93.0	91.1	89.5	87.4	82.5	96.0
Si	0.00	3.0	4.3	5.8	7.0	8.9	10.5	12.6	17.5	4.0
Si_{th}*	0.00	3.3	5.0	6.7	8.3	10.0	12.5	15.0	20.0	5.0

 * supposed Silicon content, calculated by the average Silicon content in all targets

The measured Silicon contents are in good agreement to the theoretical considerations. The differences can be explained by the lower atomic weight of Silicon and the resulting higher scattering in plasma.

4.3 Coating thickness, adhesion, surface roughness

The standard characterisation of Oerlikon Balzers includes these basic characterisations. All measurements were done on QRS substrates, for results see Table 10. Please note that the VDI standard 3198 requires a coating thickness below 5 μm for adhesion evaluation and substrate hardness above 54 HRC. Considering the coating thickness and substrate hardness do not accomplish this regulation, the adhesion values are not according to the VDI standard.

Table 10: Thickness, adhesion and surface roughness of deposited coatings

	Deposition run									
	#1	#2	#3	#4	#5	#6	#7	#8	#9	#10
Si [at%]	0.00	3.0	4.3	5.8	7.0	8.9	10.5	12.6	17.5	4.0
t_c [μm]	5.24	5.24	5.07	5.18	5.36	5.23	5.30	5.28	5.11	4.95
adhesion	2-3	3	3	2-3	2-3	2-3	2	1-2*	1-2*	2
Ra [μm]	0.25	0.29	0.29	0.30	0.31	0.26	0.29	0.27	0.29	0.28

 * these two coatings show a circular crack behaviour, different than the others

In application, the coating adhesion was no issue, so no further investigations were done on the specific behaviour of coatings with Silicon content of 12.6 at% and 17.6 at% in adhesion testing. For imagination of this behaviour, figures of the indents can be seen in appendix A.1.

In the as deposited state the coating roughness did not vary significantly. Hence, SEM investigations of the surface showed a different surface structure, especially of the droplets. With increasing Silicon content the appearance of the droplets change from spherical into flat deposits (see Figure 4.2). Also the density of droplets increases with the Silicon content. The different behaviour results by the presence of an intermetallic phase in the target material. This intermetallic phase, Cr_3Si, has different electrical properties than the solid solution. This influences the arc effects and thereby results in different evaporation behaviour. The phase diagram for Chromium Silicon is shown in the appendix A.2.

As already mentioned in chapter 3.1.3, the coating 4.0 Si-STC has a different target configuration than the other coatings. The coating 4.0 Si-STC was deposited with targets of the same chemistry on all six arc sources.
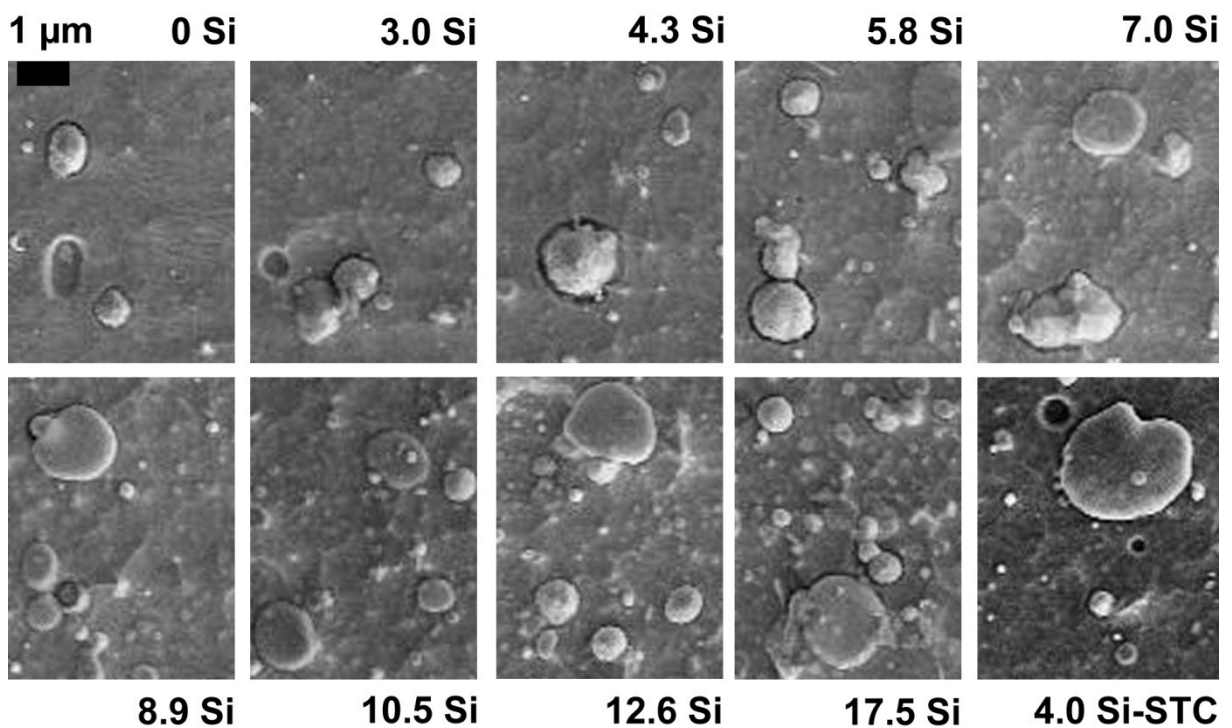

Figure 4.2: SEM surface images of QRS substrates in as deposited state.

4.4 Structure

For further discussion the coatings are termed by their Silicon content, e.g. deposition run #2 containing 3.01 at% Silicon is called "3.0 Si" and so on.

The investigation of structure was done by XRD and by SEM cross section investigations. SEM cross sections were done on QRS, SDK and THM specimens, XRD investigations were done on QRS and THM specimens. The detailed XRD patterns of all deposited coatings on THM substrates are displayed in Figure 4.5.

All deposited coatings show a face centred cubic lattice. In the XRD pattern of CrN a preferential orientation of (111) and (200) lattice planes can be observed. With addition of Si the peaks shift to smaller angles up to a Silicon content of 4.3 at%. Higher Silicon contents cause no further peak shift. At 17.5 at% Silicon the (111) and (200) peaks shift back to even higher angles than the initial CrN position.

This result can be explained by a solution of Silicon in the fcc CrN lattice up to a Silicon content of approximately 4.3 at%. In this concentration range Silicon is substitutional solved on Chromium places in the lattice. As a result, the lattice parameter increases (see Figure 4.3). Söderberg calculated in his work a lattice parameter for cubic-SiN_x (NaCl structure) of 4.20 Å [36]. These results undergird the assumption of substitution of Chromium by Silicon. At higher Silicon contents, Si_xN_y precipitations occur on triple points and grain boundaries. This process was already postulated by D. Mercs [37]. The precipitations lead to a reduction of Silicon in the unit cell. Furthermore, the precipitations on the triple points and grain boundaries obstruct the coalescence during film growth. Consequently, the grain size decreases.

Furthermore, a change in preferential orientation to (220) lattice planes can be observed. This change is special descriptive by comparison of the patterns 3.0 Si and 17.5 Si. This behaviour is also described in [38,39]. Another important change can be seen on the (422) peak, which was used for residual stress measurement by XRD. The peak broadens with increasing Silicon content. The reasons for this are described in chapter 4.5.

Additional to the as deposited state the lattice parameter was also determined after heat treatment at 800 °C for one hour. The determined lattice parameter for coating 0 Si (CrN) was 4.15037 Å and fits good with the value form the ICDD data sheet (code: 03-065-2899) of 4.1490 Å. The higher lattice parameter in the as deposited state is explained by defects, which heal out during annealing.
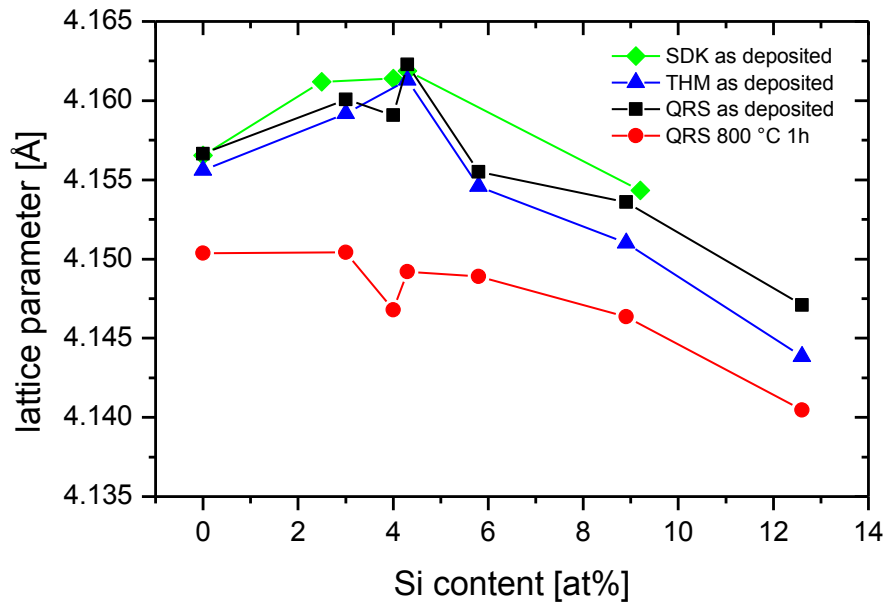
Figure 4.3: Lattice parameter development in dependence of Si content on various substrates.

In the XRD pattern of the specimen with 4.3 at% Si in Figure 4.4, it is obvious that due to heat treatment the peaks sharpen and move to higher angles. The peak shift to higher angles is explained by the relaxation of residual stresses. This is in conformity with the residual stress measurements in chapter 4.6.1. The peak sharpening is explained by grain coarsening. The results of grain size determination are given in chapter 4.5.
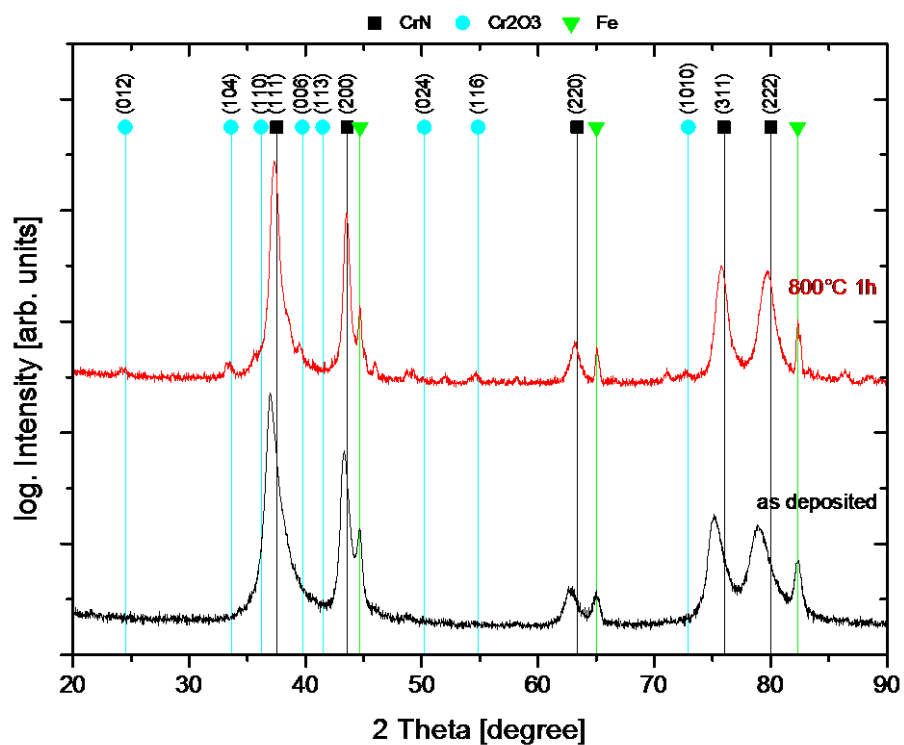

Figure 4.4: XRD pattern of 4.3 Si, measured in Bragg-Brentano arrangement in as deposited state and annealed at 800°C.
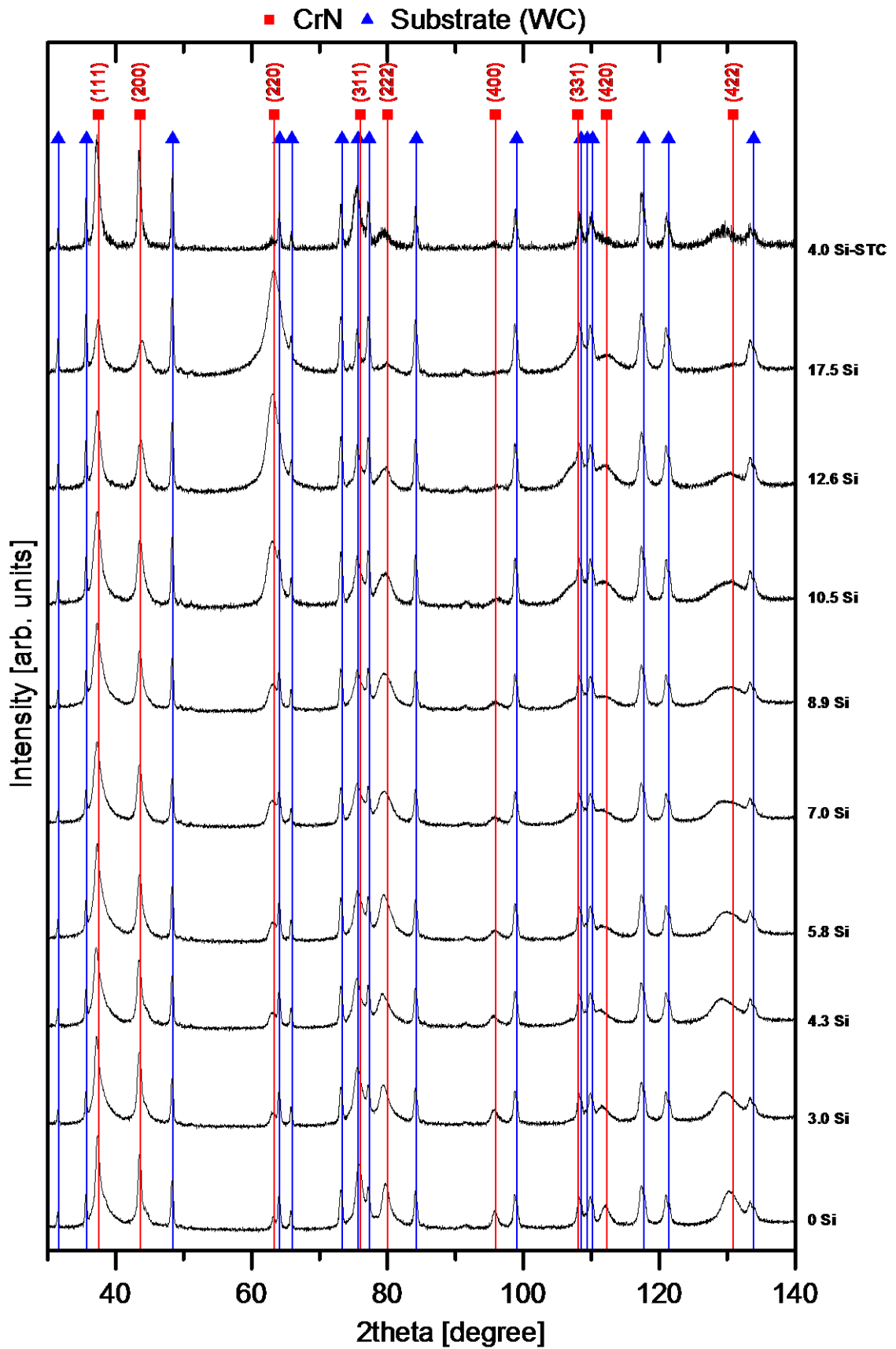
Figure 4.5: Survey Scans of Cr-Si-N coatings on THM substrates in as deposited state.

4.5 Morphology

The morphology of coatings was investigated by cross section SEM investigations. The images in Figure 4.6 show coatings with 0 at% (CrN) and 4.3 at% Silicon in the coating on QRS substrates in three different states. The comparison between these two coatings suggests a finer morphology of the Silicon alloyed coating in as deposited state. These differences are even more significant after the heat treatment of 400 °C and 800 °C for one hour. Especially after annealing at 800 °C CrN shows a coarse morphology and also a formation of an inter-layer between coating and substrate. This interlayer is less distinctive at the coating with 4.3 at% Silicon. In Figure 4.7 are more detailed images of this interlayer displayed. The thickness of this interlayer is in the case of 0 Si (CrN) approximately 900 nm and for 4.3 Si 500- 600 nm, whereby in the case for 4.3 Si the interlayer is not formed as continuously as for CrN. Investigations of coatings with higher Silicon contents did not show any trends in thickness or morphology of the interlayer.

An explanation for this observation could be the diffusion of Cr into the substrate and Fe into the coating. Si_xN_y precipitations on triple points and grain boundaries hamper the diffu-sion. Nevertheless, Chromium and Iron can diffuse via mechanism of volume diffusion. EDX line scans, which are displayed in Figure 4.8 support this theory.
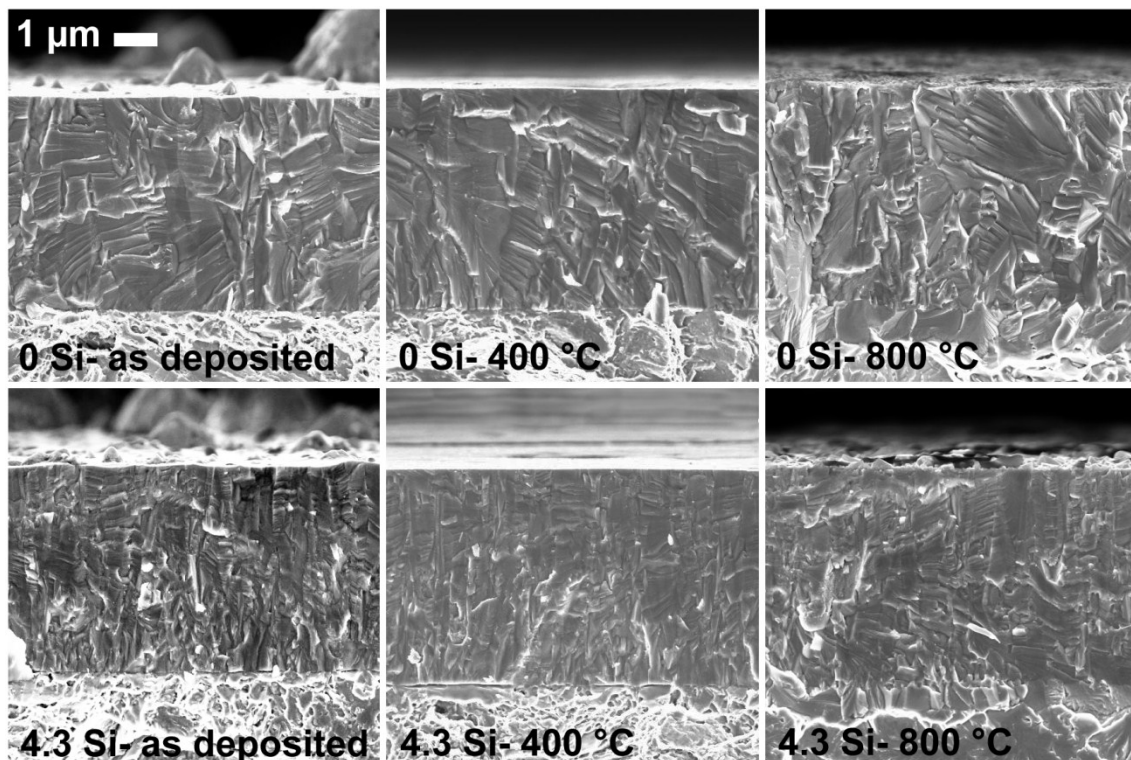

Figure 4.6: Cross section SEM images in the three different heat treatment states.
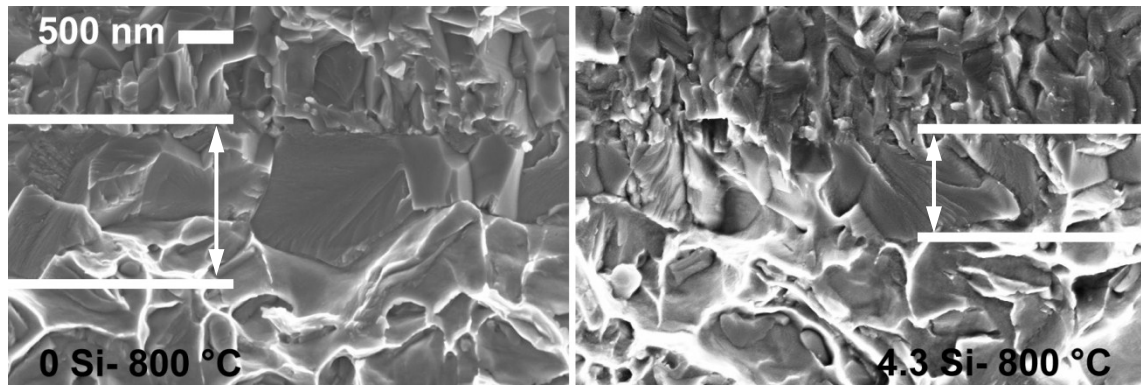
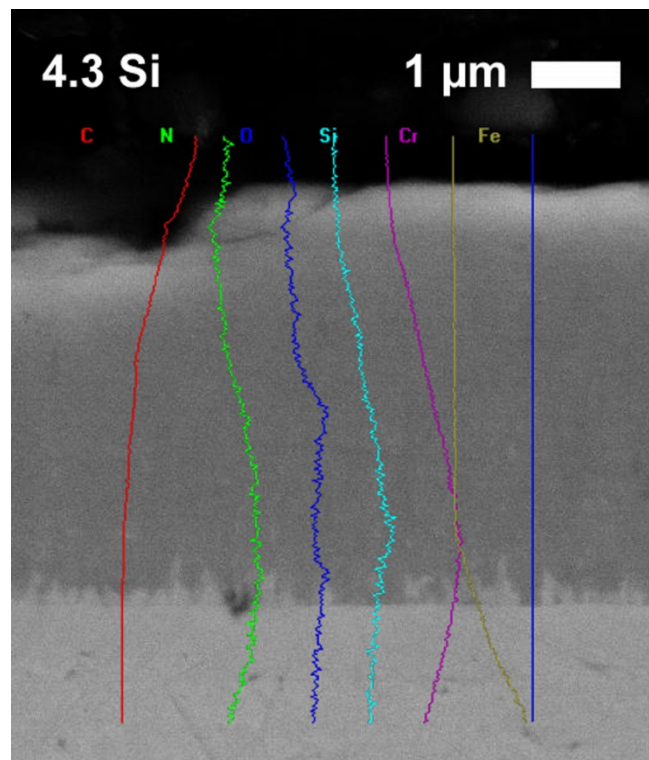Figure 4.7: Detail images of interlayer between coating and substrate.

Figure 4.8: EDX Line scan of specimen 4.3 Si after theat treatment of 800 °C for 1 hour.

Another information, which were derived from the XRD data are the grain sizes in as deposited state and after annealing at 800 °C. As written in chapter 3.2.2, the determination was done by investigation of the (111), (200) and (220) peaks. The best results were delivered by the (111) peak, which are used for Figure 4.9. The coatings with multi-layered structure show a smaller grain size as compared to the coating 4.0 Si-STC, which has a single layer structure (see target configuration, Table 4). The input energy due to heat treatment leads to a grain coarsening and an alignment at approximately 25- 30 nm. The reduction in grain size, which is observable at LUMENA, can be explained by precipitation and recrystallization. The significant higher grain size of coating 4.0 Si-STC results from the deposition configuration with the same target chemistry on all six arc sources and the resulting higher diffusivity.
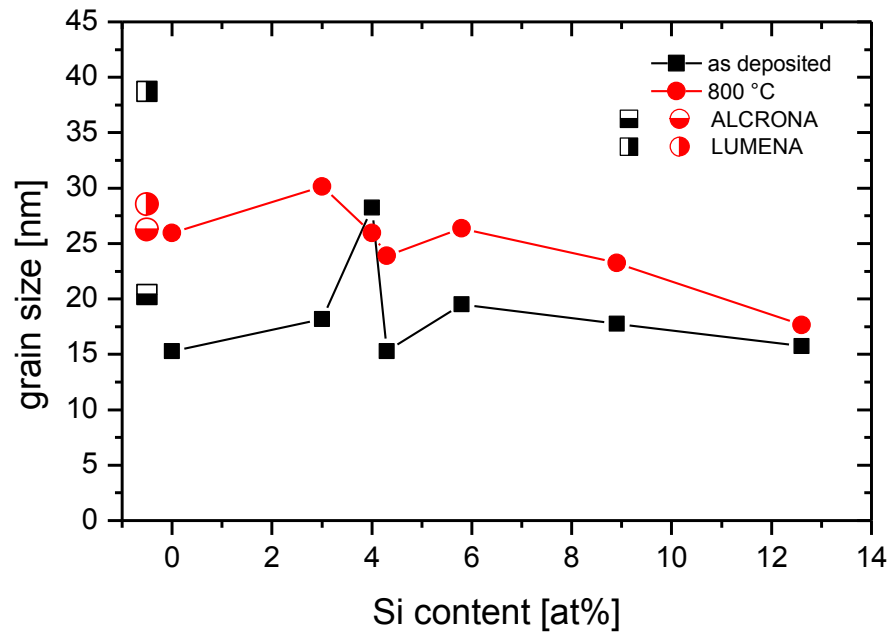
Figure 4.9: Grain sizes, calculated from (111) peak on QRS substrates in various heat treatment states. The coatings ALCRONA and LUMENA contain no Silicon.

4.6 Mechanical properties

4.6.1 Residual stress

Next to the determination of structure, the residual stresses were determined by XRD measurements. These results are strongly dependent on the substrates, as can be seen in Figure 4.11. An explanation for this behaviour is the mounting of the substrates on the carrousel by permanent magnets. A schema of the mounting situation is shown below in Figure 4.10.
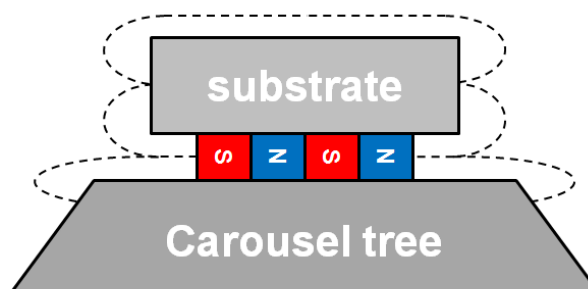
Figure 4.10: Schematic illustration of the magnetic substrate mounting on the carousel tree.

The steel grades of QRS and SDK substrates are strongly ferromagnetic, whereby the carbide of THM substrates has a much lower permeability. These reinforced magnetic fields by the ferromagnetic substrates influence the plasma close to the surface facing the sources. The most significant influence to this distinct gap is the different thermal expansion coefficient of

carbide and steel. Also a not comparable nucleation due to different grain sizes of steel and carbide may have an influence on these results.

The increase of residual stress with increasing Silicon content is explained by the solution of Silicon in the CrN lattice. The precipitation of Si_xN_y on triple points and grain boundaries leads to a reduction of residual stress, which can be obtained at a concentration above 4.0 at%. The further increase of residual stress above 5.8 at% is a consequence of the increasing amount of precipitations on triple points and along the grain boundaries.

Hence, the absolute values of these measurements are influenced by the assumptions, which were made for the calculations. Closer information of analysis is explained in chapter 3.2.2.
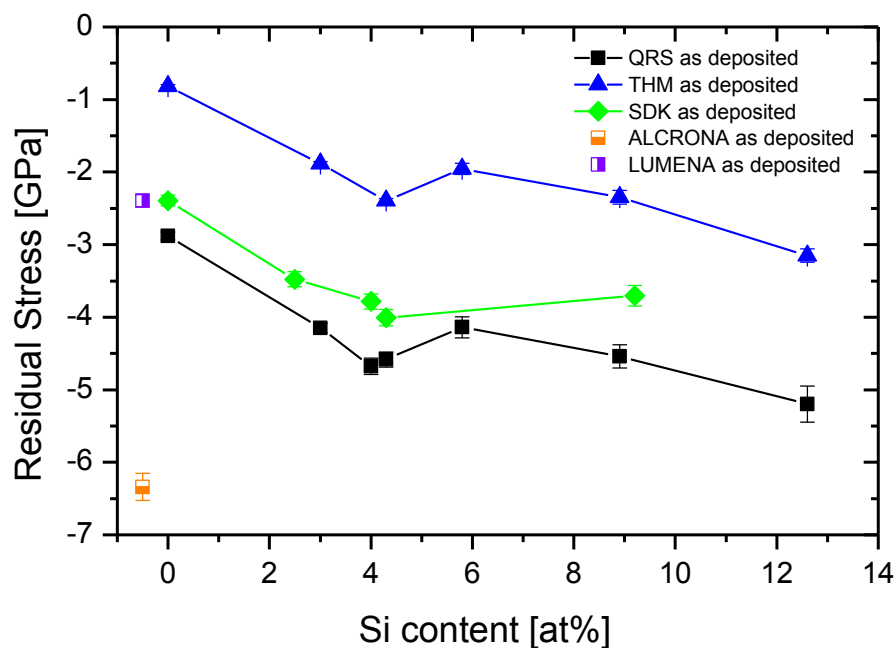

Figure 4.11: Residual stresses on various substrates in dependence of Silicon content, compared to standard coatings. The coatings ALCRONA and LUMENA contain no Silicon.

The differences in residual stress between the different substrates are also observable in cross section SEM investigations. In Figure 4.12 a comparison of the same coating between the different substrates is shown. It is obvious that the coating thickness on THM is significantly higher than on QRS and SDK substrates due to a less intense magnetic field close to the substrates surface. However, the most significant amount is caused by the different thermal expansion coefficients of THM and steel substrates. The thermal expansion coefficient of Tungsten carbide is twice as high as from CrN, whereby steel has a 5.6 times higher thermal expansion coefficient than CrN. A qualitative calculation with further data, details in appendix A.2, confirms this explanation.
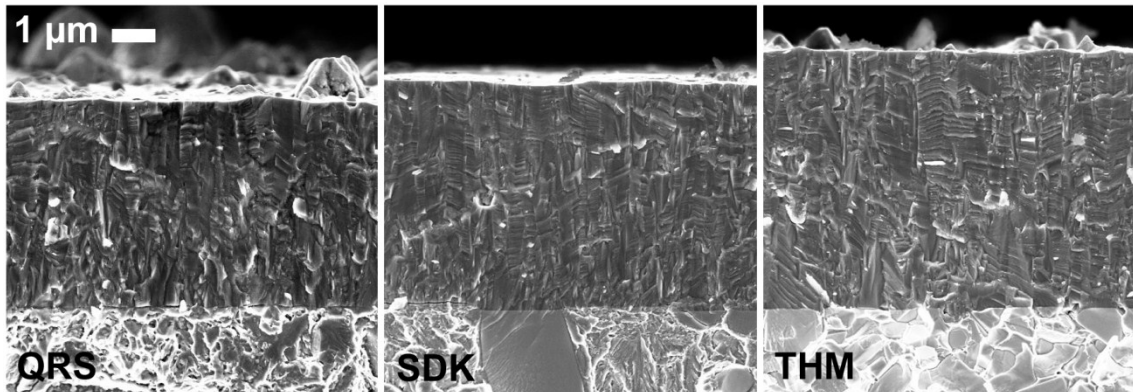
Figure 4.12: Cross section SEM images of coating 4.3 Si on the three substrates for residual stress measurements.

Next to the as deposited state, also the residual stresses after the heat treatment of 800 °C for 1 hour were investigated. On the measurement of the residual stresses after 400 °C was foregone due to the small change in XRD pattern (see, Figure 4.13), the slight change in hardness and Young's modulus (see, Figure 4.15) and the known deposition temperature of approximately 500 °C. By this reason, no significant change in residual stresses was expected. The results of residual stress measurement after annealing are displayed in Figure 4.14. The heat treatment effects a significant reduction in residual stress due to recovery processes and grain coarsening which become activated above deposition temperature.
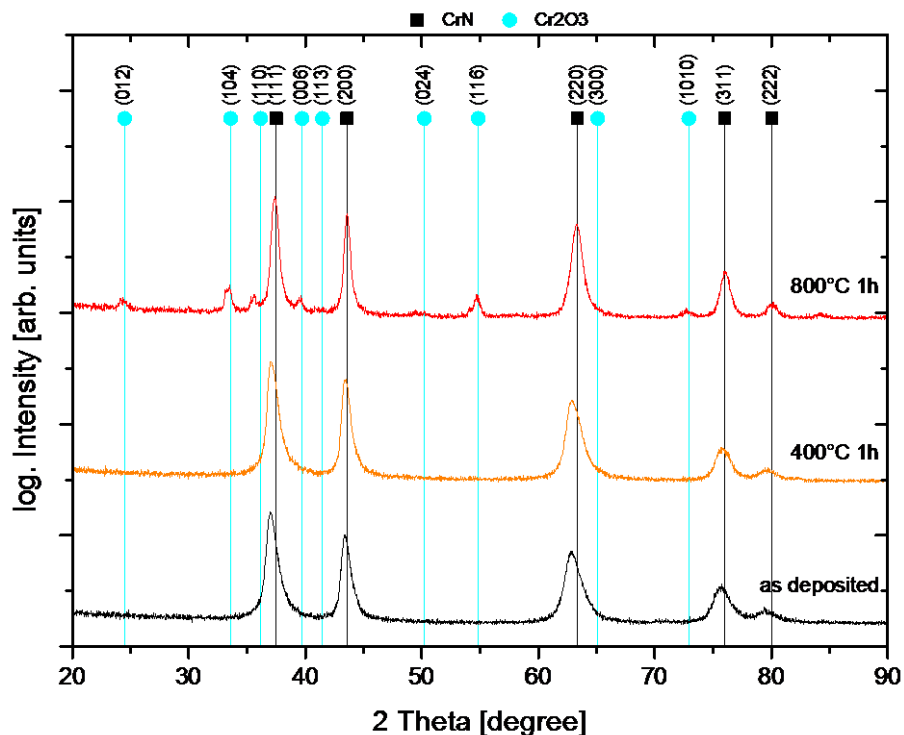

Figure 4.13: Grazing incident XRD of coating 4.3 Si in different heat treatment stages.
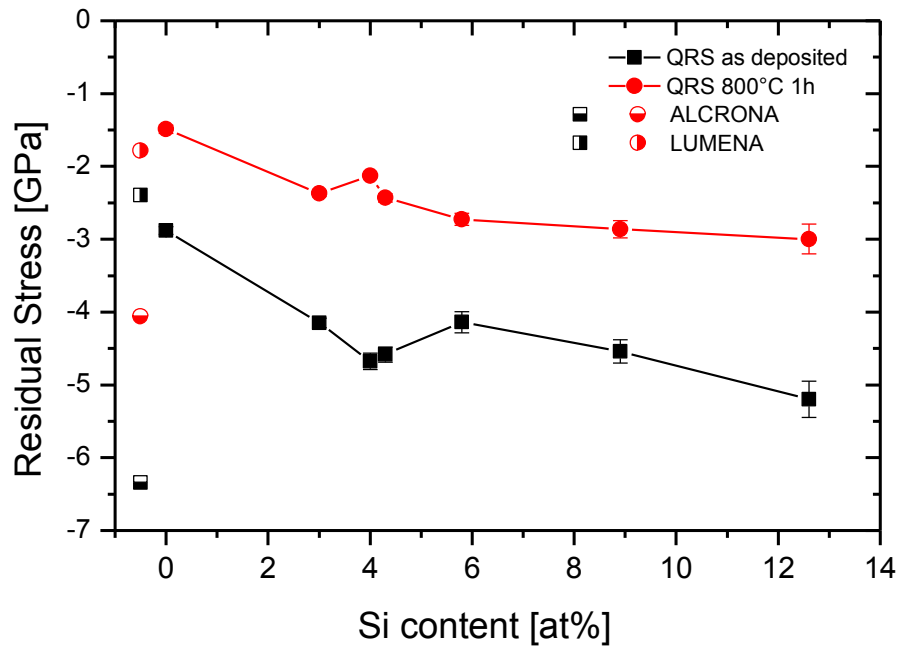
Figure 4.14: Residual stresses on QRS substrates after annealing at 800 °C for 1 hour. The coatings ALCRONA and LUMENA contain no Silicon.

4.6.2 Hardness and Young's modulus

Hardness and Young's modulus were determined in as deposited state and after annealing at ambient air at 400 °C and 800 °C for 1 hour. Thus, the stability of the coatings mechanical values in respect to thermal treatment was proven. The possibly existing oxide layers were removed by polishing the surface with a steel ball, further information in chapter 3.2.1.

The addition of Silicon to CrN leads to a significant increase in hardness and Young's modulus. As already mentioned in the chapter before, Silicon becomes solved in CrN, strains the lattice and leads by this way to an increase in hardness, respectively Young's modulus. This effect is also called solid solution hardening. Above a Silicon content of 4.3 at% the Si_xN_y precipitations lead to smaller grains, this also causes an increase in hardness. After heat treatment at 400 °C for 1 hour a reduction in hardness and Young's modulus is observable, however, this reduction is below the error of measurement. The small reduction of hardness, respectively Young's modulus can be explained by recovery processes of the coating. Evidence therefore is the slight peak sharpening after heat treatment (see Figure 4.13). A further increase in temperature up to 800 °C for 1 hour causes a further decrease in hardness and Young's modulus. The additional introduced energy enables further recovery processes and also grain coarsening, which can also be seen in the XRD pattern of Figure 4.13. Furthermore, the reduction in residual stresses leads also to a reduction in hardness, respectively Young's modulus.
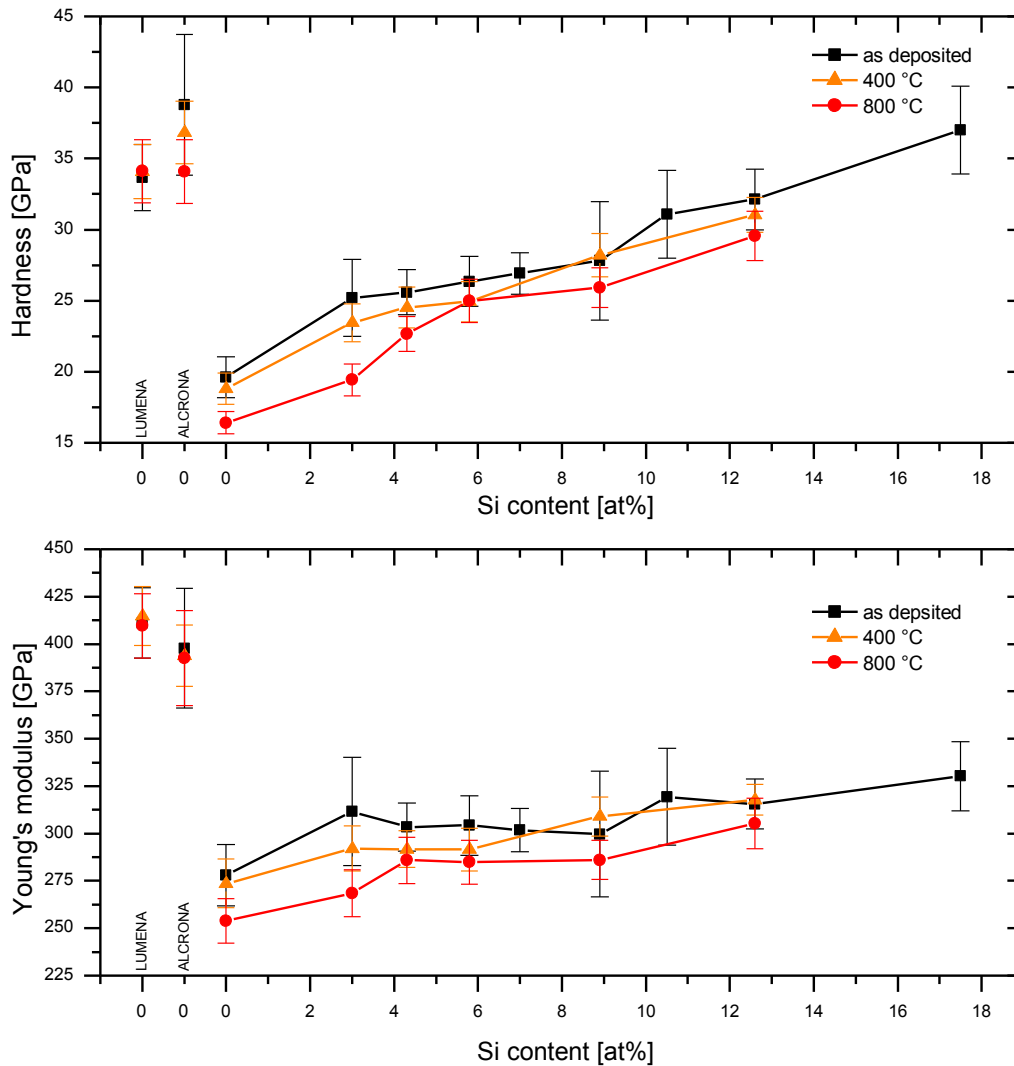
Figure 4.15: Hardness and Young's modulus on QRS substrates measured in various heat treatment states.

4.7 Tribological properties

4.7.1 Ball on Disk measurements

Ball on disk measurements at room temperature and at 800 °C were done under the same testing parameters. Next to the friction coefficient the volume of the wear track was measured and based on this data the wear coefficient was calculated for room temperature and 800 °C. This was necessary for an imagination of the high temperature wear behaviour of the coating.

In Figure 4.16 the friction coefficient for different Silicon contents is displayed as well as for the reference coatings ALCRONA and LUMENA. The coating 0 Si, i.e. CrN, a friction coefficient of ~0.3 can be observed. With addition of Silicon, the friction coefficient increases significantly up to a value of ~0.6 for the coating with 8.9 at% Si. LUMENA has an even higher friction coefficient of ~0.7, ALCRONA of approximately 0.63.

The increase of friction coefficient with increasing Silicon content can be correlated with the residual stresses and the hardness of the coatings. The alumina ball in the measurements concentrates the load on a small area. With increasing Silicon content the residual stresses and respectively the hardness, are higher compared to CrN. Thus, wear particles break out more easily from the demanded surface. These wear particles effect the increase in friction coefficient at room temperature. Especially at coating 8.9 Si a cyclic wear behaviour can be observed, which is related with the target configuration at deposition. The coating is built up from layers with high Silicon content followed by CrN layers. Due to this structure the friction coefficient varies cyclic.
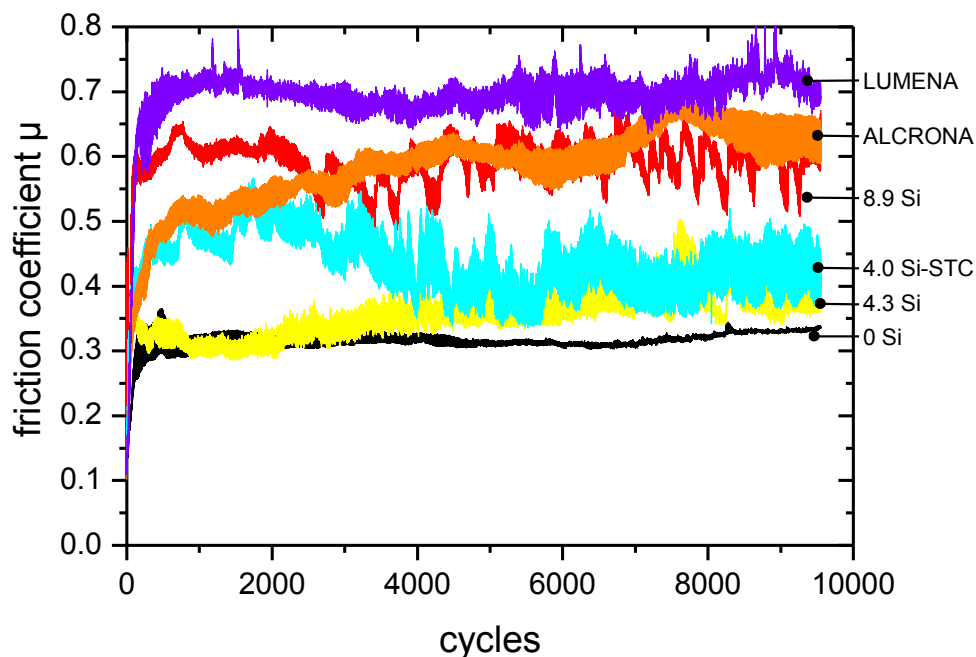

Figure 4.16: Friction coefficient of various coatings, measured at 5 N and room temperature.

The differences in friction behaviour at room temperature are not observable at 800 °C in ambient air. In Figure 4.17 the friction coefficient curves are displayed for the different coatings. Due to the formation of oxides the friction coefficient drops compared to the measurements at room temperature. For CrN the friction coefficient reaches equilibrium at ~0.25. With addition of Silicon the friction coefficient in steady state keeps in the range between 0.25 and 0.35. However, the running-in behaviour changes with increasing Silicon content. The coating with 8.9 at% Si reaches the equilibrium state quicker than the coatings with lower Silicon contents.

At the reference coatings (ALCRONA and LUMENA) a slightly different friction coefficient is observed due to different chemistry and mechanical properties of the built oxides.
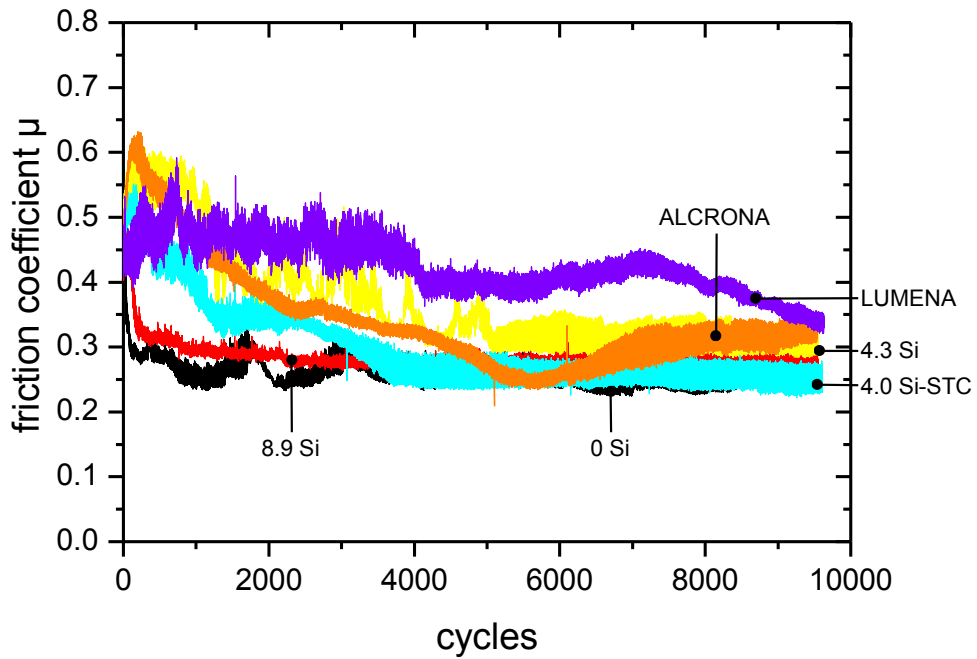
Figure 4.17: Friction coefficient of various coatings, measured at 5 N and 800 °C at ambient air.

4.7.2 Wear resistance

The wear resistance was measured by two different methods. First by the calotte grinding method, described in chapter 3.2 and second by volume measurement of the wear track on ball on disk experiments. Thereby, an imagination of the high temperature wear behaviour was given.

The results of calotte grinding method show a slight decrease of wear coefficient with increasing Silicon content, basically the wear coefficient lies on a level of $\sim 4.0 \cdot 10^{-15}$ m³/mN, see Figure 4.18. The development of wear resistance shows the same tendency as the quotient of Hardness and Young's modulus, as mentioned in [40].
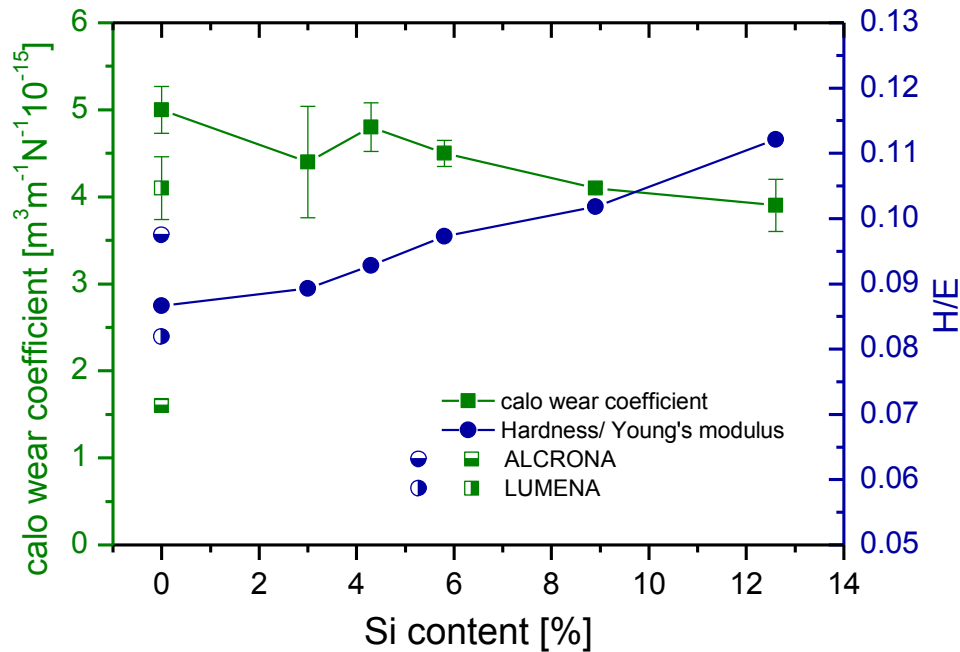
Figure 4.18: Wear coefficient determined by calotte grinding method.

Additional to these measurements the wear behaviour was determined by volume measurements on wear tracks after ball on disk measurements. The results are displayed in Figure 4.19. At room temperature the wear coefficient increases slightly with increasing Silicon content. This is in antithesis to the calotte grinding measurements. The coefficients between these two measurement methods differ about a factor of ~16. Hence, these differences have a systematic origin. In detail, the calotte grinding method is characterized by the removal of wear products by the suspension and furthermore the diamantine wear particles. Whereby in ball on disk experiment the wear products are only removed by centrifugal force and the wear particles originates from the alumina ball or the coating itself. This results in the significant higher wear coefficient measured by calotte grinding method.

At high temperatures (800 °C) the wear behaviour is strongly dependent on the formation of lubricating oxides. Coatings with Silicon content between 2.5 and 4.3 at% show significant higher wear rate.
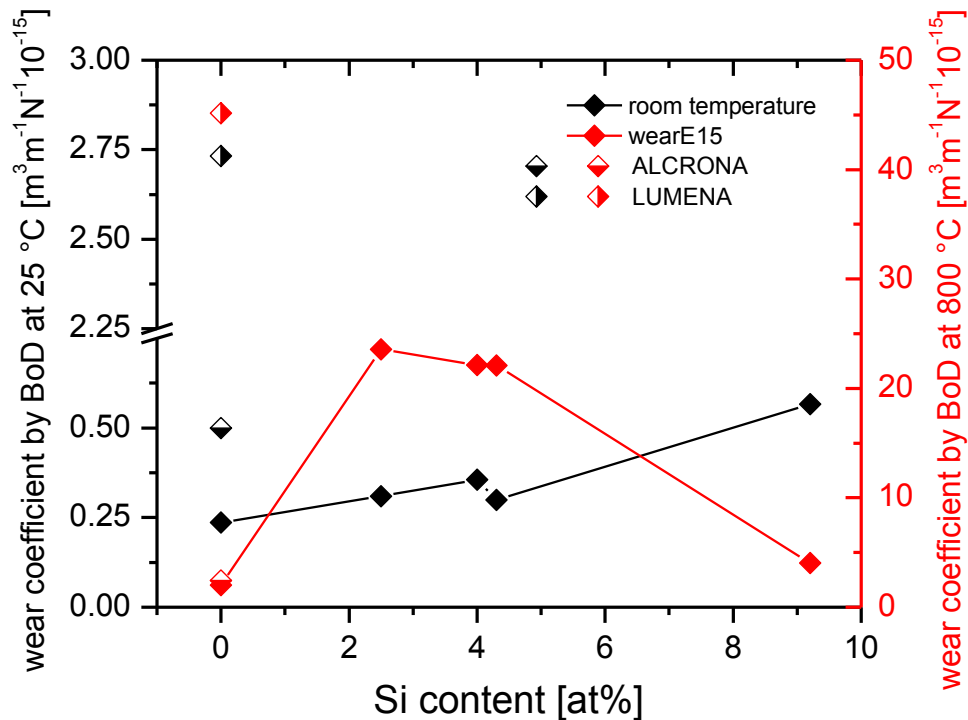
Figure 4.19: Wear coefficient determined by volume measurements on ball on disk wear tracks.

4.8 Oxidation behaviour and thermal stability

The coatings thermal stability and oxidation behaviour is an important issue for coating application, due to the point that the top layer of the coating are in direct contact with the glowing steel sheet. By this reason, coated QRS specimens become annealed in ambient air at 400 °C and 800 °C always for 1 hour.

Sputtered CrN is thermally stable up to temperatures of ca. 750 °C, which can be increased by the addition of Silicon [41,42]. In Figure 4.20 grazing incident XRD measurements on 0 Si coating (CrN) is displayed. After heat treatment of 400 °C for 1 hour no changes are observable, due to a higher deposition temperature of approximately 500 °C. At this temperature also no oxides can be identified. This behaviour changes after annealing at 800 °C. The XRD pattern shows significant Cr_2O_3 peaks. These oxides are also investigated by cross section SEM studies, shown in Figure 4.22.
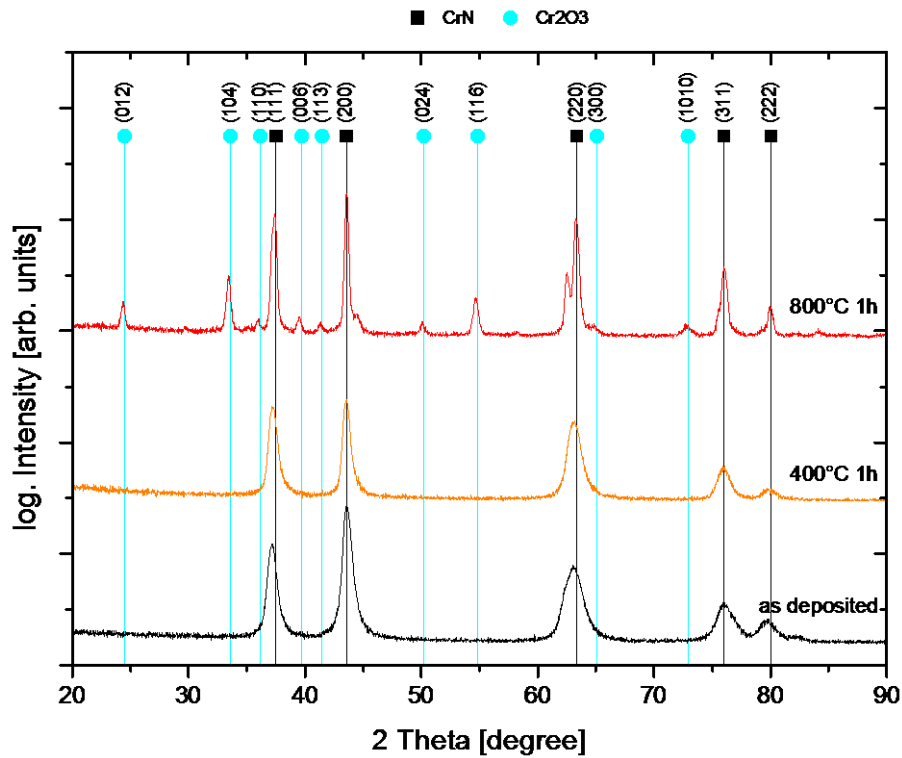
Figure 4.20: Grazing incident XRD of CrN, respectively 0 Si, at various oxidation temperatures.

The addition of Silicon leads to a higher oxidation resistance of the coating. In Figure 4.21 the grazing incidence XRD measurements of all annealed Cr-Si-N coatings are displayed. The XRD pattern shows a reduction in peak intensity for oxide peaks compared to 0 Si (CrN). Between the specimens with different Silicon contents a reduction in peak intensity of the (012) peak is observable, but the other peaks show a similar intensity. This would offer the conclusion of no further effect of Silicon on the oxidation behaviour. But, this is in contradiction to the cross section SEM investigations, shown in Figure 4.22.

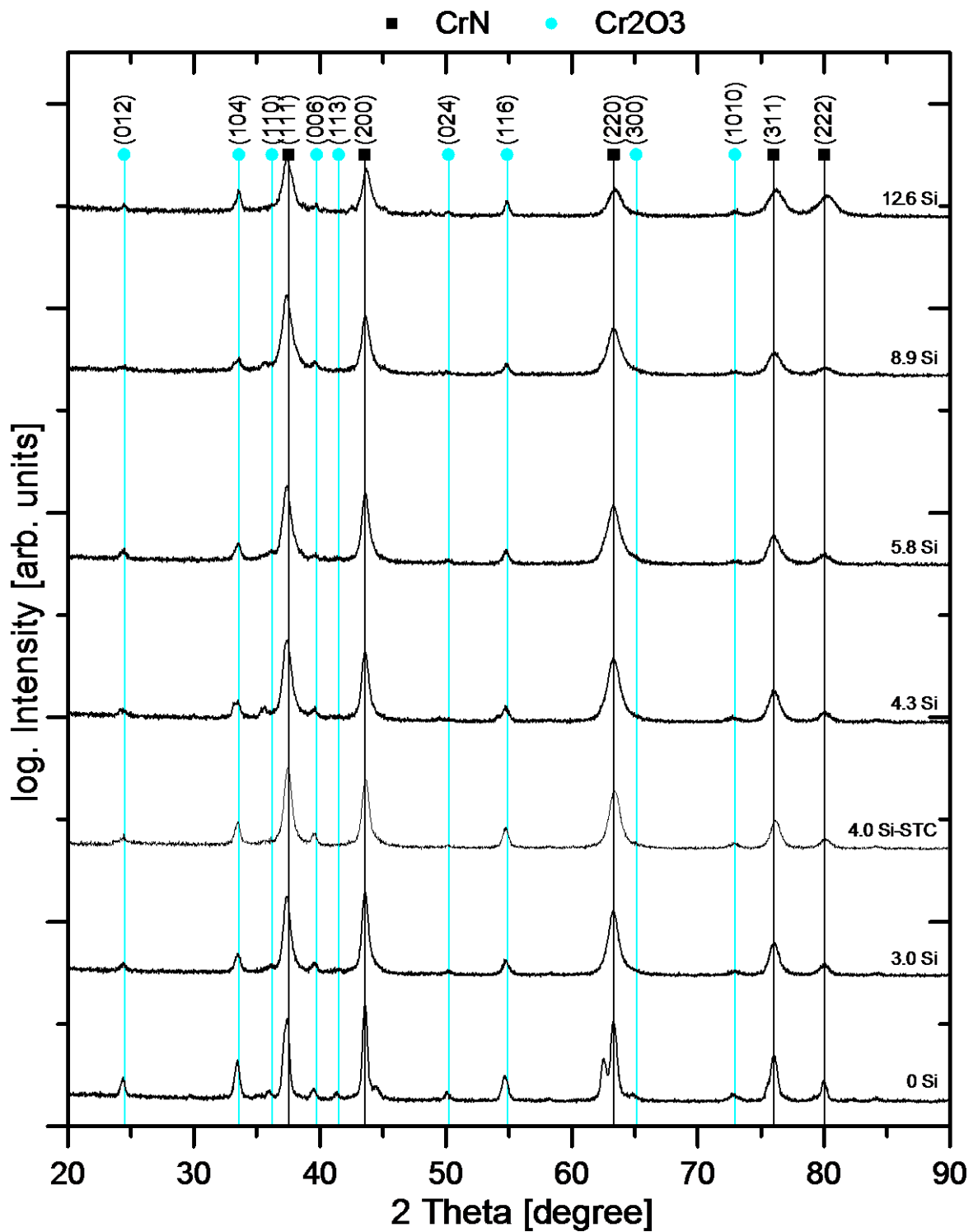Figure 4.21: Compilation of grazing incidence XRD measurements of all Cr-Si-N coatings on QRS substrates after annealing at 800 °C for 1 h in ambient air.

The reduction in oxide peak intensity reflects the increase in oxidation resistance due to the addition of Silicon to CrN, see Figure 4.22. The thickness of the oxide layer obtained from oxidised coatings on QRS substrates. An overview about these thickness measurements is

given in Figure 4.23. The displayed data of oxide layer thickness are average values from 5 to 7 measurements. The low oxide layer thickness of ALCRONA is related with the high Aluminium content in the coating, nevertheless the XRD pattern shows no peaks of alumina, see Figure A.4. The oxide layer of LUMENA shows two different morphologies, a dense top layer followed by a porous layer underneath. The corresponding XRD pattern shows no different oxides, only the peaks of TiO_2 are observable, whereby the investigated modification is Anatase (a body centred tetragonal modification of TiO_2) and not the expected Rutile. Hence, the porous layer can be related to TiO_2.
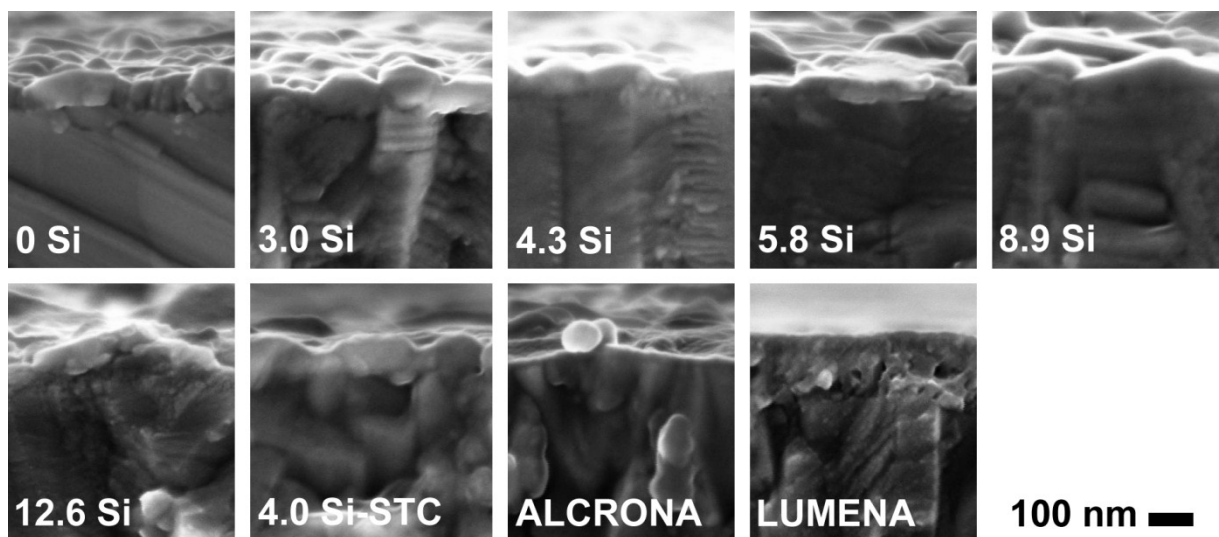

Figure 4.22: Comparison of oxide layer thickness and morphology after annealing at 800 °C for 1 h in ambient air.
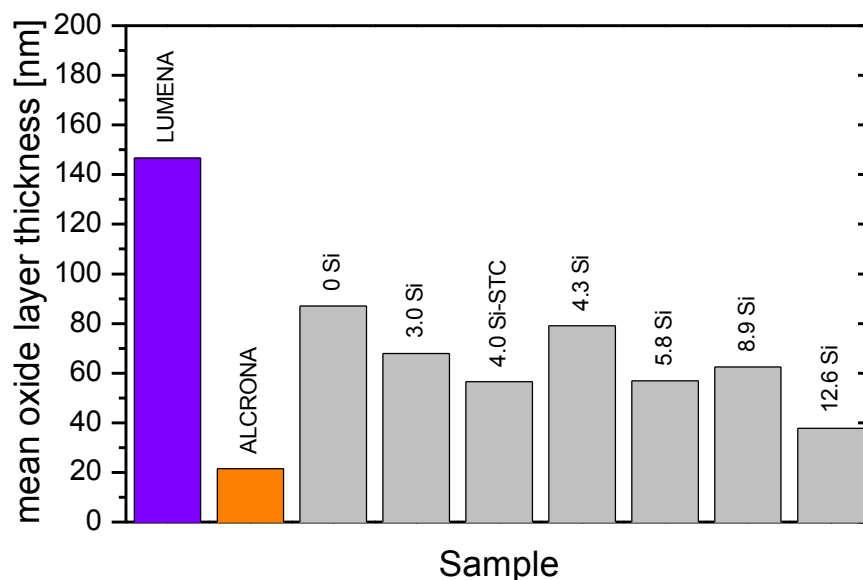

Figure 4.23: Mean oxide layer thickness after heat treatment at 800 °C for 1 hour.

4.9 Adhesive wear

4.9.1 Hardware tests

As written in chapter 3.2.4, at hardware tests several measurement data were stored. One of these data is the friction coefficient, calculated from the drawing and shearing force. However, the measured data at hardware tests do not allow a significant differentiation between the different coatings. For example the friction coefficient as a function of the shearing distance is displayed in Figure 4.24 for the most different coatings.

Compared to the other Cr-Si-N coatings, the lowest friction coefficient is observed for the coating 12.6 Si. Nevertheless, the reference coatings (ALCRONA and LUMENA) show similar friction coefficients. As it can be seen in Figure 4.26, the friction coefficient does not represent the adhesive wear in a sufficient way. Additional to the friction coefficient the area of adhesive wear was determined on the drawing jaws. The results of these measurements are displayed in Figure 4.25. An important detail in reading this graph is the different target configuration at deposition of the coating 4.0 Si-STC.
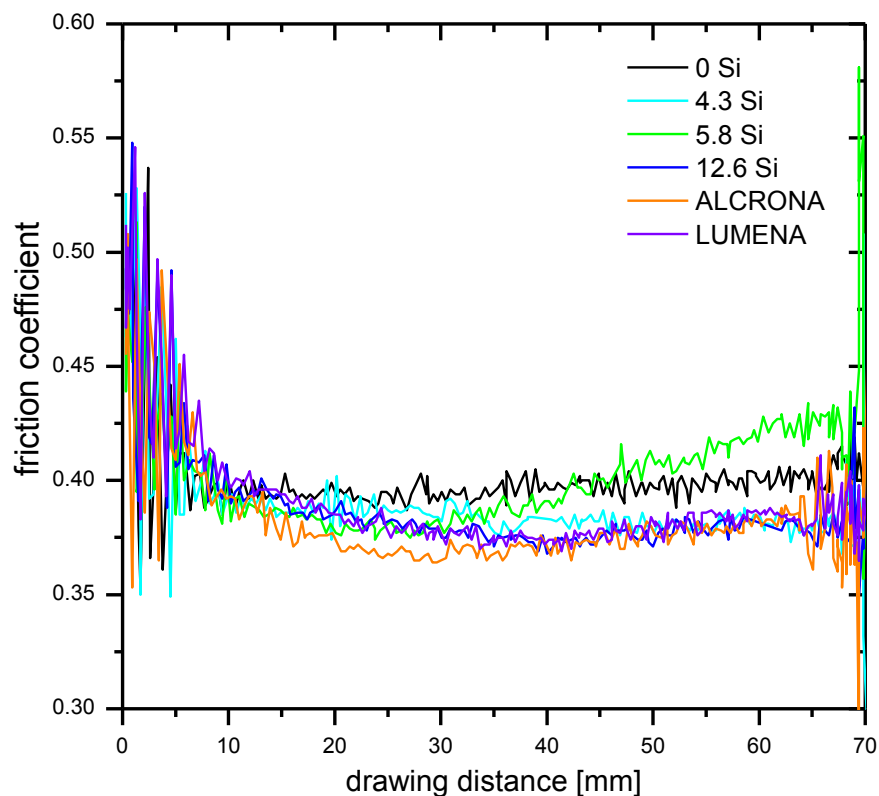

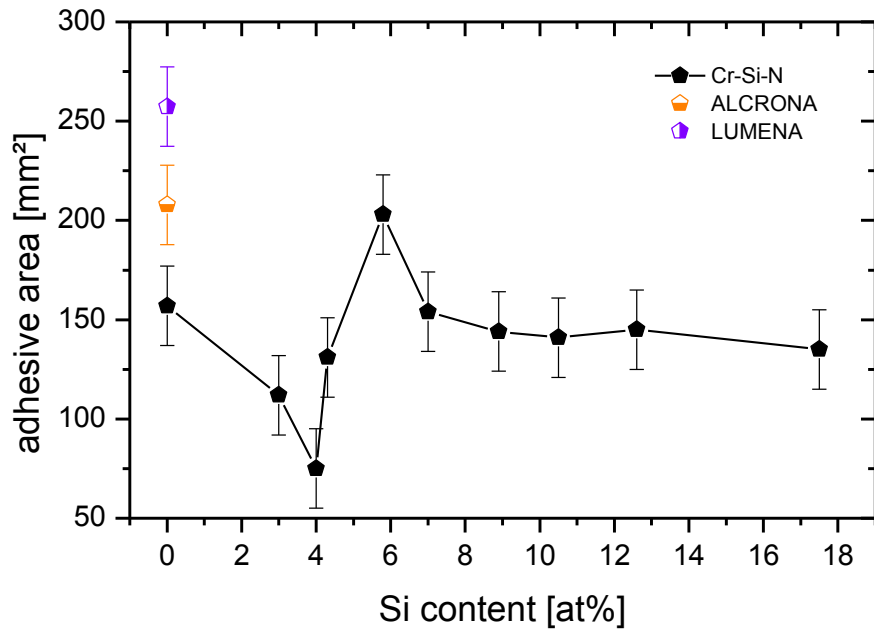Figure 4.24: Friction coefficient as a function of drawing distance at hardware tests.

Figure 4.25: Area of adhesive wear as a function of Si content.

Figure 4.26: Drawing jaws after hardware test. Each pair was tested 5 times.

4.9.2 SRV tests

The oscillation-friction-wear tester was used to determine high temperature friction and wear experiments at Oerlikon Balzers and furthermore to the adhesive wear on SRV Pins against USIBOR® steel sheet.

High temperature friction and wear experiments

For further measurements the data of SRV tester were checked by the high temperature ball on disk experiments, see Figure 4.27. Basically, the measurements show the same characteristic as the measurements by ball on disc. As in the results in ball on disk experiments (see Figure 4.17), all coating systems have a very similar friction coefficient in steady state. Nevertheless, the measured friction coefficients are not comparable with those from ball on disk. For 0 Si (CrN) a friction coefficient was measured in ball on disk of ~0.3, whereby in high temperature SRV tester a friction coefficient was measured from ~0.5. One explanation for this difference is the twice higher load in SRV tests. Furthermore, in SRV tests the time between two load cycles is shorter than in ball on disk. As a result, the lubricating oxide layer in SRV tests is not as sufficiently built up as in ball on disk measurements.

The most significant difference in wear behaviour is observable at LUMENA. In ball on disk, for LUMENA a friction coefficient of ~0.35 was observed. The wear behaviour in SRV is not comparable with the high temperature ball on disk experiments, the behaviour reminds on the friction curve of ball on disk at room temperature. This supports the explanation for the higher friction coefficient.
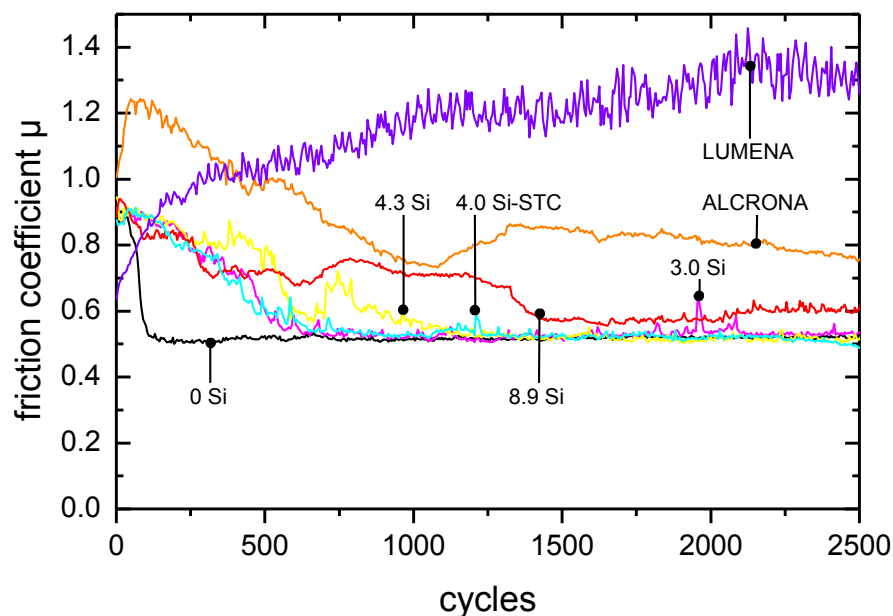

Figure 4.27: Curves of friction coefficients at 800 °C, measured in SRV tester.

Pin on USIBOR® tests

As already mentioned in chapter 3.2.3, the SRV tester offers the possibility to test special shaped pins against USIBOR® steel sheets. At this point the measured friction coefficients were compared with the data form hardware test and also among themselves.

In Figure 4.28 the measured friction coefficients are displayed for the different coatings. As already seen in hardware tests, by comparison of friction coefficient no reliable statement about the adhesive wear behaviour is possible. Furthermore, the measured friction coefficients are about the factor 2.5 higher compared to hardware test. The reasons therefore are manifold. In hardware test 5 draws were done, each cycle with a new steel sheet. In contact with the drawing jaws, the steel sheets move only in one direction. In difference therefore, in SRV experiments, the pin does almost 120 cycles on the USIBOR® sheet and claims always the same position. In the test setup of SRV test, the pin accomplishes a movement in two directions, rightwards and leftwards. As a result, the adhesive wear patterns on the pins are not completely comparable to those on the drawing jaws after hardware test. Finally, the surface roughness of pins and drawing jaws is different.
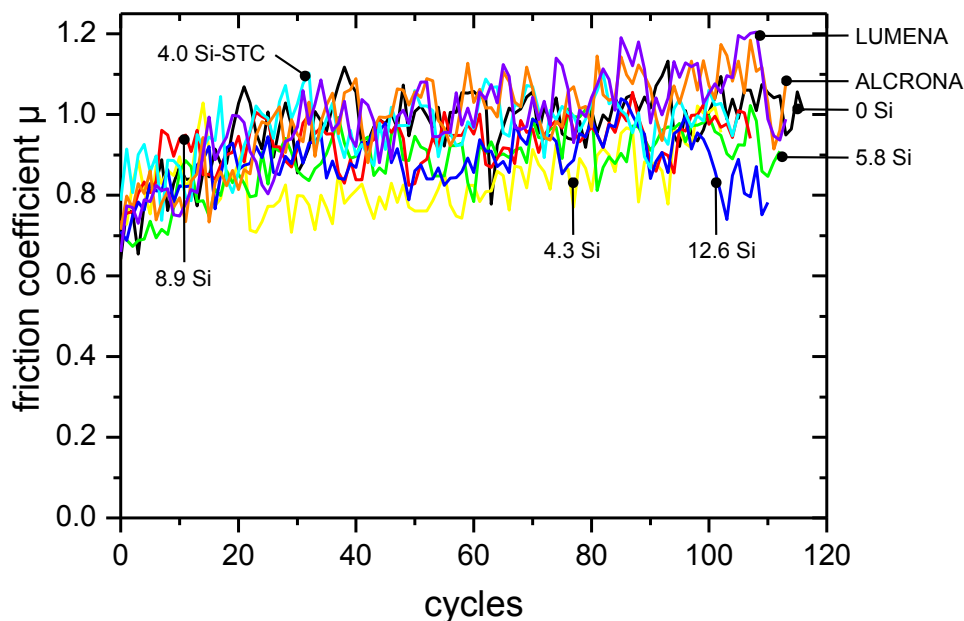
Figure 4.28: Friction coefficient in pin on USIBOR® tests at 900 °C for various coatings.

As in hardware tests, the spot of adhesive wear on the different pins was imaged. Due to the small size of the different spots, pictures were taken in SEM at low resolution. A comparison between the different coatings is shown in Figure 4.29. Therein it is clearly observable that coating 4.0 Si-STC displays the best behaviour in this test.

Figure 4.29: Comparison of the different adhesive wear spots on SRV pins after testing.

5 Conclusions

The extensive investigations of the Cr-Si-N system for application in press hardening of USIBOR® steel sheets revealed the following conclusions.

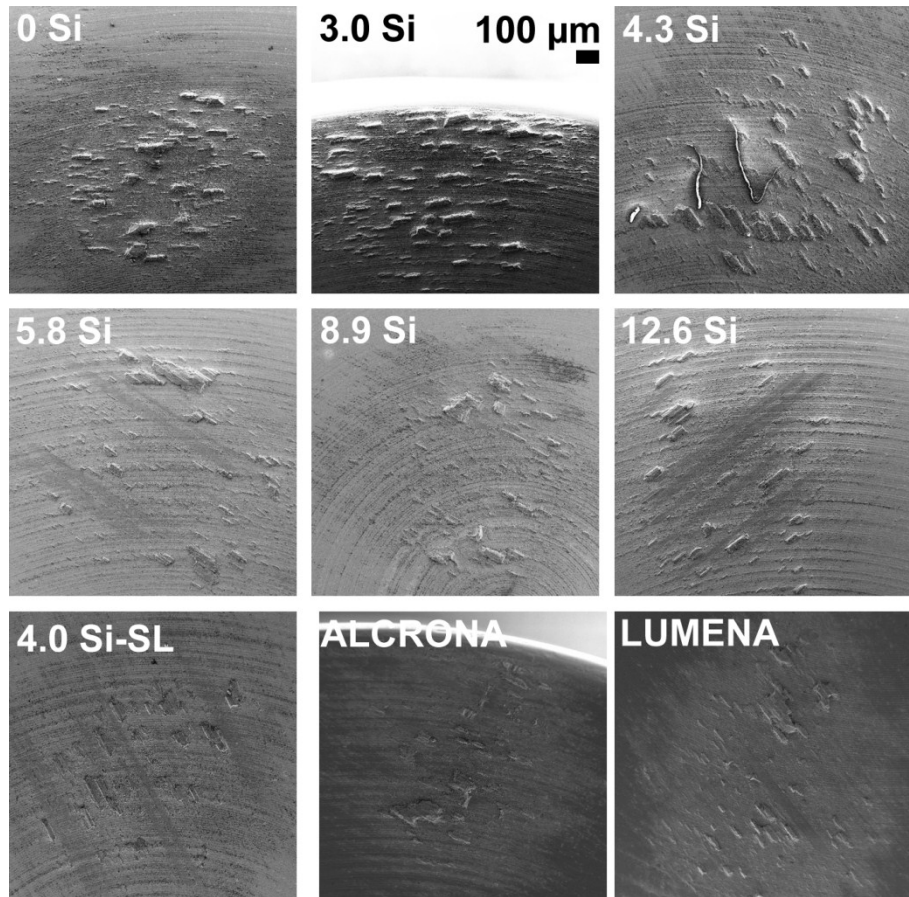The addition of Silicon to CrN results in a change from randomly orientated CrN coating to a preferential (220) orientation. This preferential orientation is most pronounced at Silicon contents above 12 at% at the metal sublattice. Furthermore, at Silicon contents above 4.3 at%, amorphous Si_xN_y starts to form during deposition, which hampers the coalescence during film growth leading to the formation of a nanostructured coating. Furthermore, the Si_xN_y phase prevents grain growth especially for coatings with a Silicon content above 12 at% up to a temperature of 800 °C. However, the coatings grain size is dependent from the target configuration in deposition process.

The residual stresses in the coatings increase with the addition of Silicon in the coating. The absolute residual stress values are strongly influenced by the difference in thermal expansion coefficient between coating and substrate. For hardness and Young's modulus also an increase from ~20 to 37 GPa and 275 to 330 GPa, respectively, with the addition of up to 18 at% Silicon is observable. The decrease in hardness and Young's modulus after annealing at 800 °C for 1 hour is below 5 and 50 GPa, respectively.

At room temperature, the friction coefficient increases with the addition of Silicon from ~0.35 up to ~0.6 for coating 8.9 Si. Furthermore, the behaviour changes form a smooth gliding for CrN to an unsteady gliding behaviour (8.9 Si). The formation of oxides at 800 °C leads to a reduction of the friction coefficient to 0.25- 0.35 for all coatings, independent of their Silicon content.

For application in press hardening, the wear resistance is of great importance. At room temperature, no significant influence of Silicon was observed on the wear resistance of the coating. In calotte grinding measurements a wear rate of $\sim 4.0 \cdot 10^{-15}$ m^3/mN was determined. The analysis of wear behaviour at 800 °C show an increased wear rate for coatings with Silicon content between 2.5 at% and 4.3at%.

Due to the high temperatures of the steel sheets in press hardening, the oxidation resistance and the high temperature stability of the coating is crucial. The cross section SEM investigations of the annealed coatings have proven the high temperature stability of the coating. Furthermore, a decrease in oxide layer thickness with increasing Silicon content was observed.

The complex processing condition, which cause adhesive wear were reproduced in two similar tests. In both measurements the coating 4.0 Si-STC, which is the coating with the homogenous target configuration at deposition, have shown the least adhesive wear. In coherence with all other investigations, the conclusion shows that a morphology with large grains is advantageous for application in press hardening processes. The further results like hardness,

oxidation resistance and wear resistance endorse an application for press hardening. However, real application tests are on-going to investigate the effectiveness of this coating system.

Literature

[1]   ArcelorMittal. (2011, June) ArcelorMittal Automotive Worldwide. [Online]. www.arcelormittal.com/automotive/products/europe/

[2]   E. Doege and B. A. Behrens, *Handbuch Umformtechnik*, 2nd ed. Heidelberg, Germany: Springer, 2010.

[3]   Isaac Newton, , * January 1643; † March 1727.

[4]   C. Mitterer, Script of the lecture "Oberflächentechnik", 2008.

[5]   R. F. Bunshah, *Handbook of hard coatings*. New York: Noyes Publications, 2001.

[6]   M. Ohring, *Material sciense of thin films*, 2nd ed. San Diego, USA: Academic Press, 2002.

[7]   K. Röll and G. Kienel, *Vakuumbeschichtung 2, Verfahren und Anlagen*. Düsseldorf, Germany: VDI Verlag, 1995.

[8]   A.J. Lichtenberg and M.A. Lieberman, *Principles of plasma discharges and materials processing*. New York, USA: John Wiley & Sons Inc., 1994.

[9]   D.L. Smith, *Thin-Film Deposition: Principles and Practice*. Boston, Massachusetts: McGraw-Hill Publishing Co, 1995.

[10]   A. Grill, *Cold plasma in materials fabrication*. New Jersey, USA: IEEE Press, 1994.

[11]   A. Anders, *Cathodic Arcs*. New York, USA: Springer Science+ Business Media, 2008.

[12]   P. C. Johnson, *Thin Film Processes II*. Boston, USA: Academic Press, 1991.

[13]   OC Oerlikon Balzers AG, 2009.

[14]   P. M. Martin, *Handbook of Deposition Technologies for Films and Coatings: Science, Applications and Technology*, 3rd ed. Oxford, UK: Elsevier Inc., 2010.

[15]   G. A. Mesyats, *Explosive Electron Emission*. Ekaterinburg, Russia: URO Press, 1998.

[16]   G. A. Mesyats, *Cathode Phenomena in a Vacuum Discharge: The Breakdown, the Spark and the Arc*. Moscow, Russia: Nauka, 2000.

[17]   M. B. Bochkarev, "Ecton processes of low current vacuum arc imaged with streak technique," in *21th Int.Symp. Discharges and Electrical Insulation in Vacuum*, Yalta, Ukraine, 2004, pp. 241-244.

[18]   P. H. Mayrhofer, *PhD thesis*. Leoben, Austria: Department of Physical Metallurgy

and Materials Testing, University of Leoben, 2001.

[19] I. Petrov, P. B. Barna, L. Hultman, and J. E. Greene, "Microstructural evolution during film growth," *Journal of Vacuum Science and Technology A*, vol. 21, no. 5, 2003.

[20] R. Rachbauer, *Diploma Thesis*. Leoben, Austria: Department of Physical Metallurgy and Materials Testing, University of Leoben, 2008.

[21] B. A. Movchan and A. V. Demchish, *Physics of Metals and Metallography*, vol. 28, no. 4, pp. 83-90, 1969.

[22] J. A. Thornton, "High Rate Thick Film Growth," *Annual Review of Materials Science*, vol. 7, pp. 239-260, 1977.

[23] R. Messier, A. P. Giri, and R. A. Roy, "Revised structure zone model for thin film physical structure," *Vaccum Science Technology A*, vol. 2, no. 2, pp. 500-503, 1984.

[24] A. Reiter, *PhD Thesis*. Leoben, Austria: Department of Physical Metallurgy and Materials Testing, University of Leoben, 2009.

[25] H. R. Stock and A. Schul, *DIN-Fachbericht 39: Charakterisierung dünner Schichten*, 1st ed., H. Jehn, G. Reiners, and N. Siegel, Eds. Berlin, Germany: Beuth Verlag, 1993.

[26] NanoFocus AG, *Manual µsurf®*. Oberhausen, Germany.

[27] H. Bückle, *Metallurgical Reviews*, no. 4, p. 49, 1959.

[28] W. C. Oliver and G. M. Pharr, "An improved technique for determining hardness and elastic modulus using load and displacement sensing indentation experiments," *Journal of Materials Research*, no. 7, pp. 1564- 1583, 1992.

[29] A. C. Fisher-Cripps, *Nanoindentation*. New York, USA: Springer Science + Business Media, 2004.

[30] L. Spieß, G. Teichert, R. Schwarzer, H. Behnken, and C. Genzel, *Moderne Röngtenbeugung*, 2nd ed. Wiesbaden, Germany: Vieweg+Teubner | GWV Fachverlage GmbH, 2009.

[31] F. Rovere, *Theoretical and experimental assessment of Cr-Al-Y-N as protective coating for y-TiAl based alloys*. Germany: Shaker Verlag GmbH, 2010.

[32] U. Welzl, J. Ligot, P. Lamparter, A. C. Vermeulen, and E. J. Mittemeijer, "Stress analysis of polysrystalline thin films and surface regions by X-ray diffraction," *Journal of Applied Crystallography*, November 2004.

[33] S. A. Speakman. (2011, April) MIT Center for Material Science and Engineering. [Online]. http://prism.mit.edu/xray

[34] OPTIMOL Instruments, *Manual of SRV Test System*. Munich, Germany.

[35] A. Ademaj, "Evaluation of coating systems for hot-sheet-metal," METAKUS, Baunatal, Germany, Measurement report 2010.

[36] H. Söderberg, M. Odén, L. Hultman, and H. M. Molina-Aldareguia, "Epitaxial stabilization of cubic-SiNx in TiN/SiNx multilayers," *Applied Physics Letters*, no. 88, p. 191902, 2006.

[37] D. Mercs, N. Bonasso, S. Naamane, Jean-Michel Bordes, and C. Coddet, "Mechanical and tribological properties of Cr-N and Cr-Si-N coatings reactively sputter deposition," *Surface & Coatings Technology*, no. 200, pp. 403-407, 2005.

[38] L. Castaldi et al., "High temperature phase changes and oxidation behaviour of Cr-Si-N coatings," *Surface & Coating Technology*, no. 202, pp. 781-785, 2007.

[39] H. Y. Lee et al., "The synthesis of CrSiN film deposition using magnetron sputtering system," *Surface & Coatings Technology*, no. 200, pp. 1026-1030, 2005.

[40] P. H. Mayrhofer, C. Mitterer, and J. Musil, "Structure-property realationship in single- and dual-phase nanocrystalline hard coatings," *Surface and Coating Technology*, no. 174-175, pp. 725-731, September-October 2003.

[41] J. W. Kim, K. H. Kim, D. B. Lee, and J. J. Moore, "Study on high-temperature oxidation behaviours of Cr-Si-N films," *Surface & Coating Technology*, no. 200, pp. 6702-6705, 2006.

[42] A. Thobor-Keck et al., "Influence of silicon addition on the oxidation resistance of CrN coatings," *Surface & Coating Technology*, no. 200, pp. 264-268, 2005.

[43] École Polytechnique de Montréal, Génie chimique. (2011, April) CRCT. [Online]. http://crct.polymtl.ca/FACT/documentation/SGTE/SGTE_Figs.htm

[44] R. E. Hummel, *Electronic Properties of Materials*, 3rd ed. New York, USA: Springer Science+Business Media, LLC, 2005.

A Appendix

A.1 Adhesion testing

According to the results in chapter 4.3, the microscopic images of HRC indents are displayed. Image (a) shows a usual indent with the crack network and scattered delamination, in image (b) the special adhesion behaviour of Cr-Si-N at high Silicon content is displayed. There are no cracks or delamination observable at the indent edge of Run 9 (Cr-Si$_{17.55at\%}$-N). Hence, there is a circular crack around the indent in greater distance to the indent edge. Therefore, this crack was not considered at adhesion characterisation.
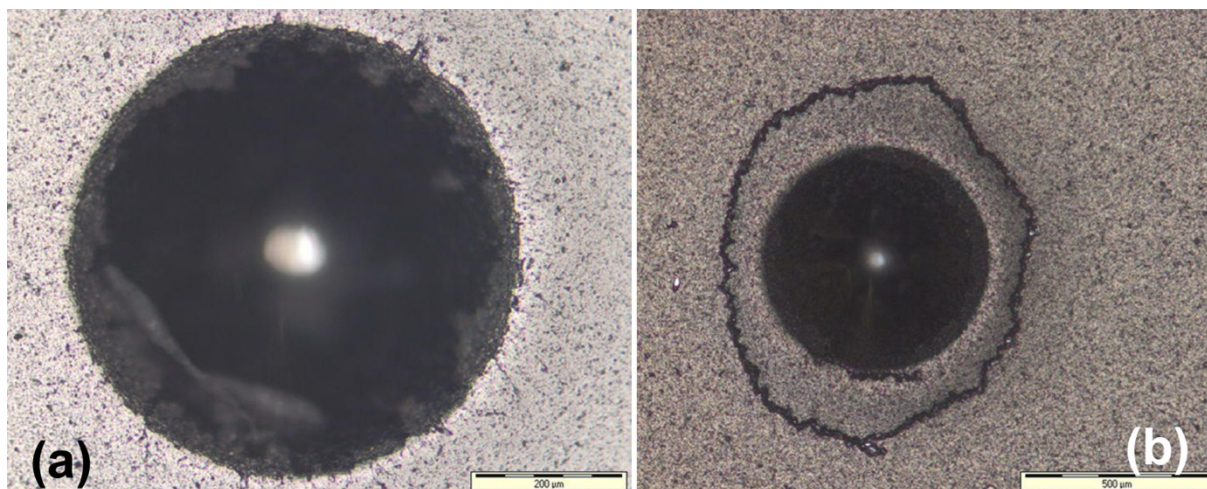

Figure A.1: Image (a) shows the HRC indent of 5.8 Si; image (b) shows the indent of 17.5 Si.

A.2 Phase diagram of Cr/Si targets

In chapter 3.1.3 already written, three different compositions of Cr/Si targets are used. These three compositions are Cr/Si 95/5, Cr/Si 90/10 and Cr/Si 80/20 at%. In the phase diagram of Figure A.2 the presence of the intermetallic phase, Cr$_3$Si, can be seen in the target with 20 at% Silicon.
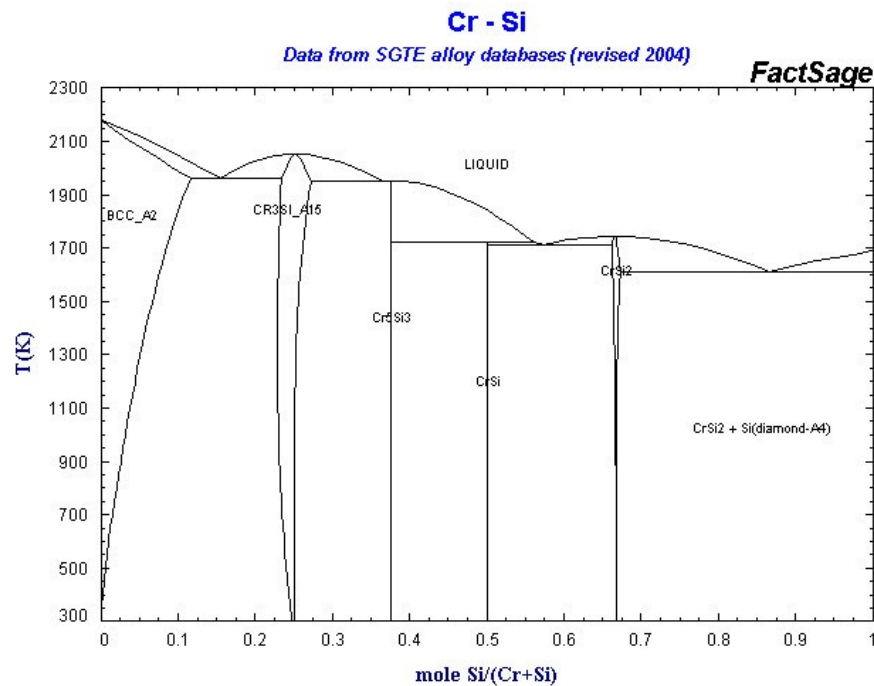
Figure A.2: Phase diagram of the Chromium Silicon system [43].

A.3 Thermal induced residual stresses

The calculation of thermal induced residual stresses was done according to the formula,

$$\sigma_{thermal} = \frac{(\alpha_s - \alpha_f) \cdot \Delta T \cdot E}{1 - \upsilon_f},$$

[6]

whereby, α_s and α_f are the thermal expansion coefficients of substrate and coating, ΔT is the temperature difference between deposition temperature and room temperature (25 °C), E is the Young's modulus, measured by micro-indentation and υ_f is the Poisson's ratio of the coating. The Poisson's ratio was calculated from the roentgenographic constant S1 and the measured Young's modulus, according to the formula form [32]. For calculation material data were used from literature [9], in detail this means.

$$\alpha_s(WC) = 4.3 \cdot 10^{-6} \, K^{-1}$$
$$\alpha_s(Steel) = 12.9 \cdot 10^{-6} \, K^{-1}$$
$$\alpha_f(CrN) = 2.3 \cdot 10^{-6} \, K^{-1}$$
$$\Delta T = 475 \, K$$
$$S_1(CrN) = -0.77 \, TPa^{-1}$$
$$\upsilon_f = -S_1 \cdot E$$

Based on this material data, a thermal induced residual stress was calculated. In Figure A.3 the results are displayed as a function of Silicon content for the two different substrates, THM and QRS. In this calculation the difference between THM and QRS substrates is over all

compounds ~ 1.5 GPa. The remaining difference of ~0.5 GPa is caused by the high variance of the measured Young's modulus values. Furthermore, the use of Young's modulus values measured on QRS in calculation for THM cause also a systematic failure as well as the standard values of thermal expansion coefficients. However, the calculation is still in good agreement with the measured data.
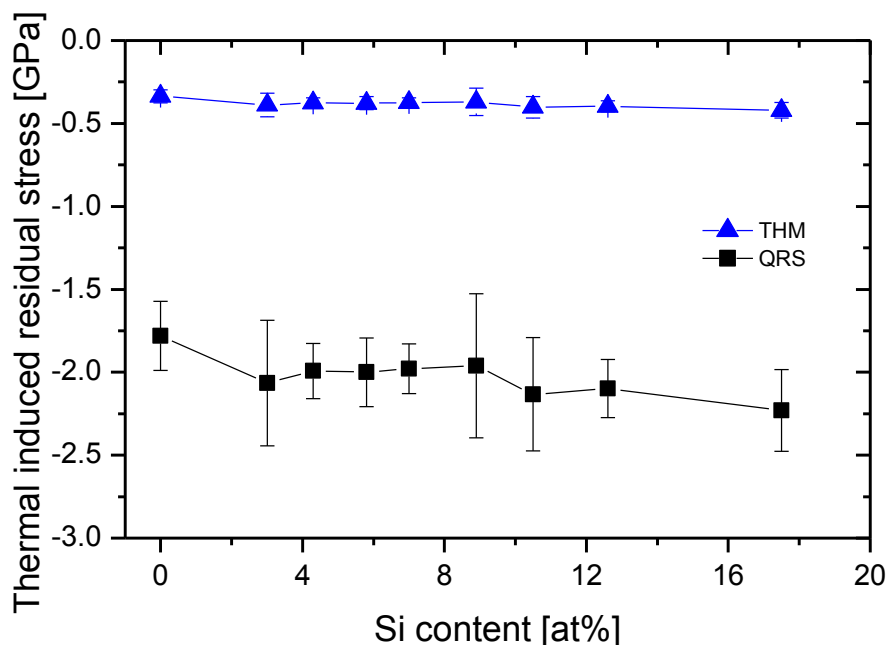

Figure A.3: Induced thermal stresses as function of the silicon content for QRS and THM substrates.

A.4 Grazing incidents XRD pattern of ALRONA and LUMENA

Additional to the Cr-Si-N coatings, the oxidation behaviour of ALCRONA and LUMENA was also investigated. The grazing incidence XRD patterns are shown in Figure A.4 and Figure A.5.
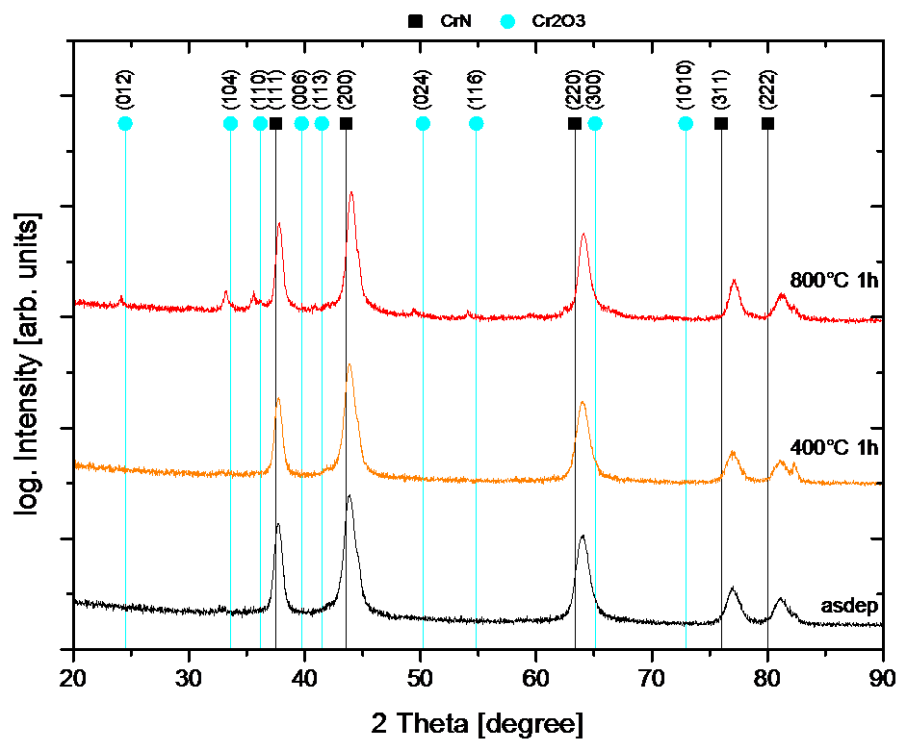
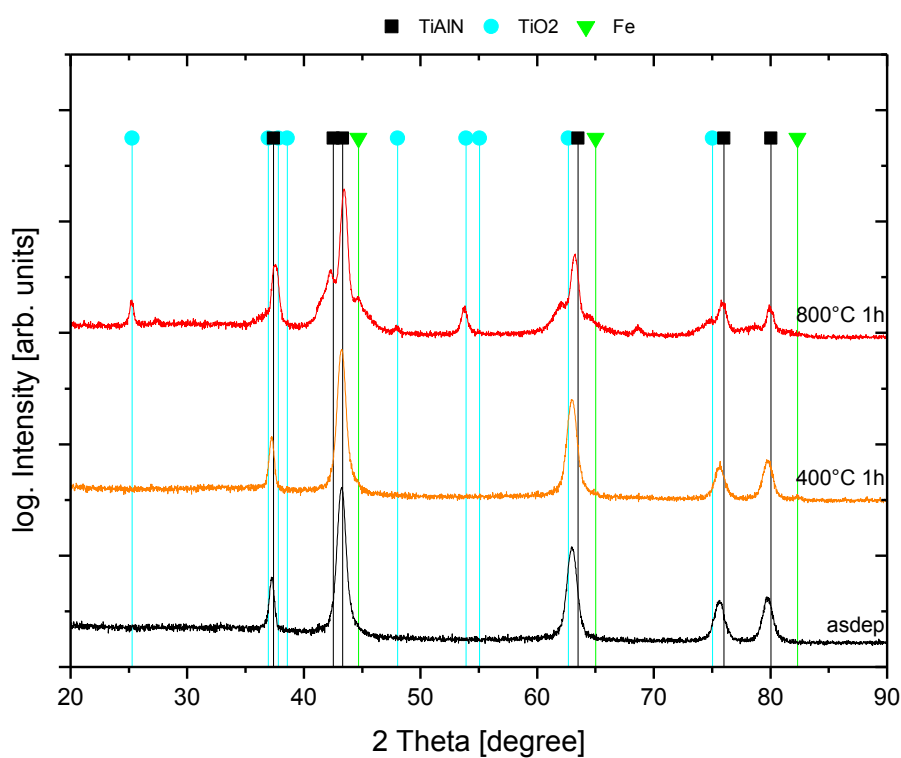Figure A.4: grazing incident XRD pattern of ALCRONA in the three heat treatment stages.

Figure A.5: grazing incident XRS pattern of LUMENA in the three heat treatment stages.